JAMES | Journal of Advances in Modeling Earth Systems

RESEARCH ARTICLE
10.1029/2021MS002696

Effect of a Scale-Aware Convective Parameterization Scheme on the Simulation of Convective Cells-Related Heavy Rainfall in South Korea

Haerin Park[1], Gayoung Kim[1], Dong-Hyun Cha[1], Eun-Chul Chang[2], Joowan Kim[2], Sang-Hun Park[3], and Dong-Kyou Lee[4]

[1]Department of Urban & Environmental Engineering, Ulsan National Institute of Science and Technology, Ulsan, South Korea, [2]Department of Atmospheric Sciences, Kongju National University, Kongju, South Korea, [3]Department of Atmospheric Sciences, Yonsei University, Seoul, South Korea, [4]School of Earth and Environmental Sciences, Seoul National University, Seoul, South Korea

Key Points:

- We investigated the impact of the scale-aware convective parameterization scheme (CPS) across the gray-zone using the Weather Research and Forecasting model
- The scale-aware CPS improved simulated convective cells related to rainfall by properly removing atmospheric instability in the gray-zone
- Convective available potential energy timescale and entrainment rate modulated in the Multiscale Kain–Fritsch are the key parameters for the improved rainfall simulation in the gray-zone

Supporting Information:

Supporting Information may be found in the online version of this article.

Correspondence to:

D.-H. Cha,
dhcha@unist.ac.kr

Citation:

Park, H., Kim, G., Cha, D.-H., Chang, E.-C., Kim, J., Park, S.-H., & Lee, D.-K. (2022). Effect of a scale-aware convective parameterization scheme on the simulation of convective cells-related heavy rainfall in South Korea. *Journal of Advances in Modeling Earth Systems*, *14*, e2021MS002696. https://doi.org/10.1029/2021MS002696

Received 23 JUL 2021
Accepted 14 MAY 2022

Abstract In this study, the effect of a scale-aware convective parameterization scheme (CPS) on the simulation of heavy precipitation in the gray-zone was investigated using the Weather Research and Forecasting (WRF) model. We performed WRF simulations with the Kain–Fritsch (KF) scheme (non-scale-aware), Multiscale Kain–Fritsch (MSKF) scheme (scale-aware), and explicit convection (i.e., no CPS). The MSKF scheme uses a scale-aware parameter that modulates the convective available potential energy (CAPE) timescale and entrainment process in the KF scheme as a function of the horizontal grid spacing. The results of this study show that WRF simulations using explicitly resolved convection lead to overestimations and erroneous precipitation locations in the gray-zone because the convection and atmospheric instability cannot be appropriately triggered and reduced. The CPS without scale-awareness in the gray-zone exaggerates the convection and distorts synoptic fields, leading to the erroneous simulation of heavy precipitation at high resolution. The MSKF scheme with scale-awareness improves the simulation of convective cells-related heavy rainfall by removing the atmospheric instability in the gray-zone, reducing the role of the CPS, and increasing the role of the microphysics parameterization scheme (MPS) with decreasing grid spacing. In addition, the results of sensitivity experiments show that reducing the CAPE timescale leads to the faster development of convective cells, whereas decreasing the entrainment leads to precipitation overestimation. The modulated parameters in the scale-aware MSKF scheme play a crucial role in balancing the effects of the CPS and MPS in the gray-zone.

Plain Language Summary Based on the increase in computational resources, numerical weather prediction models are operating in the "gray-zone" for horizontal grid spacing in the range of 1–10 km in which both cumulus parameterizations and explicitly resolved deep convection are problematic. In this study, the effect of the scale-aware convective parameterization scheme (CPS) on the simulation of convective cell-related heavy precipitation across the gray-zone was investigated using the Weather Research and Forecasting (WRF) model. The scale-aware CPS uses a scale-aware parameter, which modulates the convective process as a function of the horizontal grid spacing. We found that simulating convection processes in the gray-zone without the CPS is inadequate. Furthermore, the CPS without scale-awareness generates an erroneous precipitation simulation due to the exaggeration of convection and distortion of synoptic fields. In contrast, the scale-aware CPS improves the simulation of convection cell-related heavy rainfall in the gray-zone by reducing the role of the CPS and increasing that of explicitly resolved precipitation with the decrease in the grid spacing. Our results indicate that using a scale-aware CPS and managing convective processes are crucial in controlling the CPS and microphysics parameterization scheme (MPS) in the gray-zone.

1. Introduction

More than half of the annual precipitation in Korea is concentrated in the summer (Ho & Kang, 1988; Park et al., 2008). Heavy rainfall during the summer monsoon is one of the most prominent characteristics of precipitation in Korea, which causes considerable socioeconomic damage (Kang et al., 1992; Lee et al., 2017; Seo et al., 2011). Based on the Korean Ministry of the Interior and Safety, the average number of annual deaths and the total property damage caused by heavy rainfall between 2009 and 2018 were 11.5 people and $125 million,

respectively (MOIS, 2019). The rainfall characteristics in Korea have been altered due to climate change. Ha et al. (2005) and Kwon et al. (2007) showed that the East Asian summer monsoon has changed since the early mid-1990s and several other studies have shown that the annual rainfall in Korea has increased since then. The frequency and intensity of precipitation have significantly increased since the 1990s (Choi et al., 2013; Kim et al., 2008; Kim & Suh, 2008; Mun et al., 2019). Choi et al. (2008) showed that the precipitation, especially in July and August, significantly increased. Lee, Kim, and Heo (2011) indicated that the total annual rainfall notably increased between 2001 and 2010 compared to the total annual rainfall between 1970 and 2000. Ho et al. (2003) showed that the precipitation intensity in early August was significantly enhanced due to the spatial difference in mid-level geopotential height over the whole of Asia as a result of global warming. Various precipitation systems generate heavy rainfall over the Korean Peninsula (e.g., band-type and cluster; Cho & Lee, 2006; Shin & Lee, 2005; Sun & Lee, 2002). Mesoscale convective systems (MCSs) are major heavy rainfall systems that are present over the Korean Peninsula during the summer monsoon period. Approximately 47% of the heavy rainfall events between 2000 and 2006 were associated with MCSs (Lee & Kim, 2007). However, more reliable and accurate predictions as well an improved understanding of the formation and development of these mechanisms based on observation data and numerical models are necessary to reduce the damage caused by heavy rainfall in Korea.

In numerical models in many previous studies, a coarse horizontal grid spacing was utilized relative to the actual horizontal scale of cumulus convection due to computing resource limitations. At coarser resolutions (e.g., grid spacing >10 km), the convective parameterization scheme (CPS) has been implemented to represent the effect of subgrid-scale convection on large-scale fields based on the calculation of the potential amount of subgrid-scale cloud formation and the physics of precipitation processes associated with grid-scale variables. By implementing the CPS, subgrid-scale convection is possible, even if the air parcel at the grid point is not saturated. Therefore, the CPS reduces the precipitation delay or removes local instabilities and represents the interaction between the clouds and surrounding environment (Bechtold et al., 2014; Freitas et al., 2018; Han et al., 2011). The results of numerous studies showed that, among other factors (e.g., domain setup, model grid size, and convective environment), numerical simulations are sensitive to the chosen parameterization scheme (Wang & Seaman, 1997; Yang et al., 2000). Jankov et al. (2007) and Lowrey and Yang (2008) indicated that different parameterization schemes (e.g., CPS and microphysics parameterization scheme, MPS) yield different simulation results; specifically, the CPS has a significant effect on the precipitation simulation.

Due to a substantial increase in the numerical computing power and improvements to atmospheric modeling technology, numerical simulations of the atmosphere at kilometer or sub-kilometer scales are now possible (Charles et al., 2009; Davies et al., 2005; Saito et al., 2006). Generally, the higher the resolution is, the more realistic is the representation of the terrain or ground surface. However, it is difficult to define the range of convection processes between the subgrid-scale, which can be parameterized using the CPS, and the grid-scale, which must be explicitly resolved (Hong & Dudhia, 2012; Jeworrek et al., 2019; Molinari & Dudek, 1992). This range is called the "gray-zone" (1–10 km; Hong & Dudhia, 2012). Therefore, the development of a CPS for the gray-zone in numerical models remains problematic.

Bryan et al. (2003) showed that a grid spacing with an order of magnitude of ∼100 m is necessary to adequately simulate convective processes. However, such a resolution is not currently feasible for regular use to simulate real-world convective events. Therefore, it is generally accepted that a CPS is not required at a grid spacing below ∼5 km (Jee & Kim, 2017; Liang et al., 2019; McMillen et al., 2015). It is assumed that the grid-scale dynamics and microphysics at this resolution are sufficient for the simulation of the general characteristics of deep moist convection. Molinari and Dudek (1992) and Weisman et al. (1997) showed that convection-permitting models explicitly simulate convection without relying on a CPS with a horizontal grid spacing below 4 km. Yu et al. (2010) indicated that a grid size of 3 km is sufficient to resolve the convection band and that a CPS is unnecessary at this resolution.

However, the results of several studies showed that the simulation of convective processes with high-resolution numerical models using explicitly resolved convection is limited (Arakawa et al., 2016; Gustafson et al., 2013). In some cases, the use of a CPS at these resolutions can improve the results. For example, Deng et al. (2006) showed that the precipitation simulations on a 4 km grid improved when a CPS was used. Furthermore, Lee, Lee, and Chang (2011) showed that heavy rainfall forecasts of numerical models improved based on the activation of both the CPS and MPS at fine grid sizes (e.g., 3 km). Thus, despite improvements at high resolution, the results are ambiguous and it remains unclear if the use of a CPS at a grid spacing below 4 km is beneficial.

Therefore, the CPS validity in the gray-zone must be adjusted or improved (Arakawa et al., 2011; Bengtsson & Körnich, 2016; Gerard et al., 2009; Grell & Freitas, 2014; Han & Hong, 2018; Hong & Dudhia, 2012; Park, 2014; Prein et al., 2015; Yun et al., 2017; Zheng et al., 2016). Such improved schemes are designed to be scale-aware such that they can represent the smooth transition between grid spacings. For this purpose, the role of the CPS is gradually reduced to reproduce the smooth reduction of subgrid-scale precipitation with increasing resolution. Sims et al. (2017) showed that a scale-aware parameter, which is a function of the horizontal resolution, controls the simulation performance of mesoscale convection phenomena and the Kain–Fritsch scheme (KF) modified by the scale-aware parameter improves the convection timing of the mesoscale convection phenomenon in the Carolinas region. Kwon and Hong (2017) applied scale-aware parameters to the Simplified Arakawa–Schubert scheme at a resolution of 3 km, which improved the simulation of summer monsoon-induced precipitation over the Korean Peninsula. Jeworrek et al. (2019) included five domains with different horizontal model resolutions (27, 9, 3, 1, and 0.3 km) in their study to investigate the performances of scale-aware CPSs in the gray-zone. They showed a significant improvement of the location, pattern, and intensity of precipitation at high resolution.

Similarly, the representation of the subgrid precipitation process plays an essential role in the simulation of precipitation over the Korean Peninsula. The results of previous studies showed that the importance of smooth CPS activation using scale-aware parameters increases with increasing resolution (Alapaty et al., 2012; Jeworrek et al., 2019; Kwon & Hong, 2017; Sims et al., 2017). Various numerical studies have been conducted to understand the effect of high-resolution models on the simulation of heavy rainfall events over the Korean Peninsula (Hong & Lee, 2009; Kwon & Hong, 2017). However, there is a lack of studies of the role of scale-aware parameterization schemes in the gray-zone in case of heavy rainfall. Therefore, the effects of scale-aware parameters on a gray-zone domain were investigated in this study using non-scale-aware and scale-aware CPSs. A single case of heavy rainfall, which comprised a flash flood event in the central region of the Korean Peninsula from July 15 to 17, 2017, was analyzed. In this study, the KF (Kain, 2004) and the Multi-scale KF (MSKF) schemes (Zheng et al., 2016) were selected for the CPSs. The MSKF scheme is a scale-aware version of the KF scheme in which the convective available potential energy (CAPE) timescale and entrainment rate are adjusted based on the horizontal grid spacing. The single case was spatially and temporally localized and thus suitable for the analysis of the precipitation sensitivity to the applied non-scale-aware and scale-aware CPSs in the gray-zone.

Simulations of numerical models are affected by various variables in the CPS such as the CAPE timescale and entrainment rate. The CAPE timescale plays a role in the dissipation of the deep moist convection instability and determines the cloud lifetime (Mishra & Srinivasan, 2010). The entrainment rate changes the convective process by determining the levels of saturation and mixing with the surrounding dry air (Khairoutdinov & Randall, 2006; Kuang & Bretherton, 2006; Lin & Arakawa, 1997). Accordingly, sensitivity experiments were conducted to examine the effects of the scale-aware CAPE timescale and entrainment rate on the precipitation simulated with the MSKF scheme.

The remainder of the manuscript is organized as follows: The heavy-rainfall case and design of the numerical experimental are described in Section 2. The results of the numerical experiments with different CPSs and sensitivities to the scale-aware CAPE timescale and entrainment rate are presented in Section 3. The summary and conclusions are provided in Section 4.

2. Case and Experimental Design

2.1. Characteristics of the Cheong-ju Rainfall Case

A significant amount of extreme precipitation was recorded in Cheong-ju, with maximum daily rainfall of 290.2 mm, and the rainfall started at 2000 UTC on July 15 (0500 LST, July 16) and the first and second peaks occurred at 2300 UTC on July 15 and 0200 UTC on July 16, respectively (Figure 1b). The hourly rainfall rates peaked at 2300 UTC, with 86.2 mm hr^{-1}, and 0200 UTC, with 67.5 mm hr^{-1}. Subsequently, the rainfall almost stopped at 0300 UTC on 16 July 2017.

Figure 2 shows the synoptic fields at four pressure levels from the final analysis (FNL) 0.25° reanalysis data at 1800 UTC, 15 July 2017, that is, 6 hr before the maximum precipitation intensity was reached in Cheong-ju. At 200 hPa (Figure 2a), an upper-pressure trough developed west of the Shandong Peninsula and a shallow upper-pressure ridge was generated south of the Shandong Peninsula, which extended to South Korea. Figures 2b and 2d show that the western North Pacific subtropical high expanded to the Korean Peninsula, forming a region

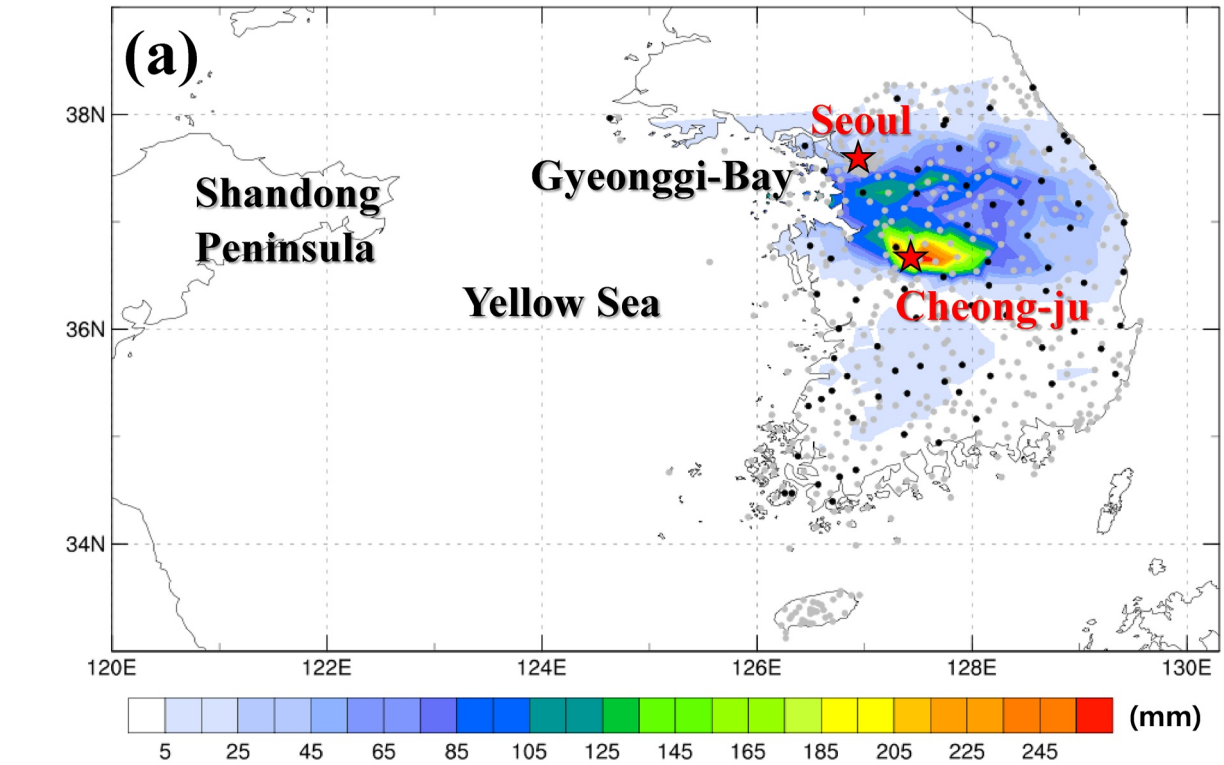

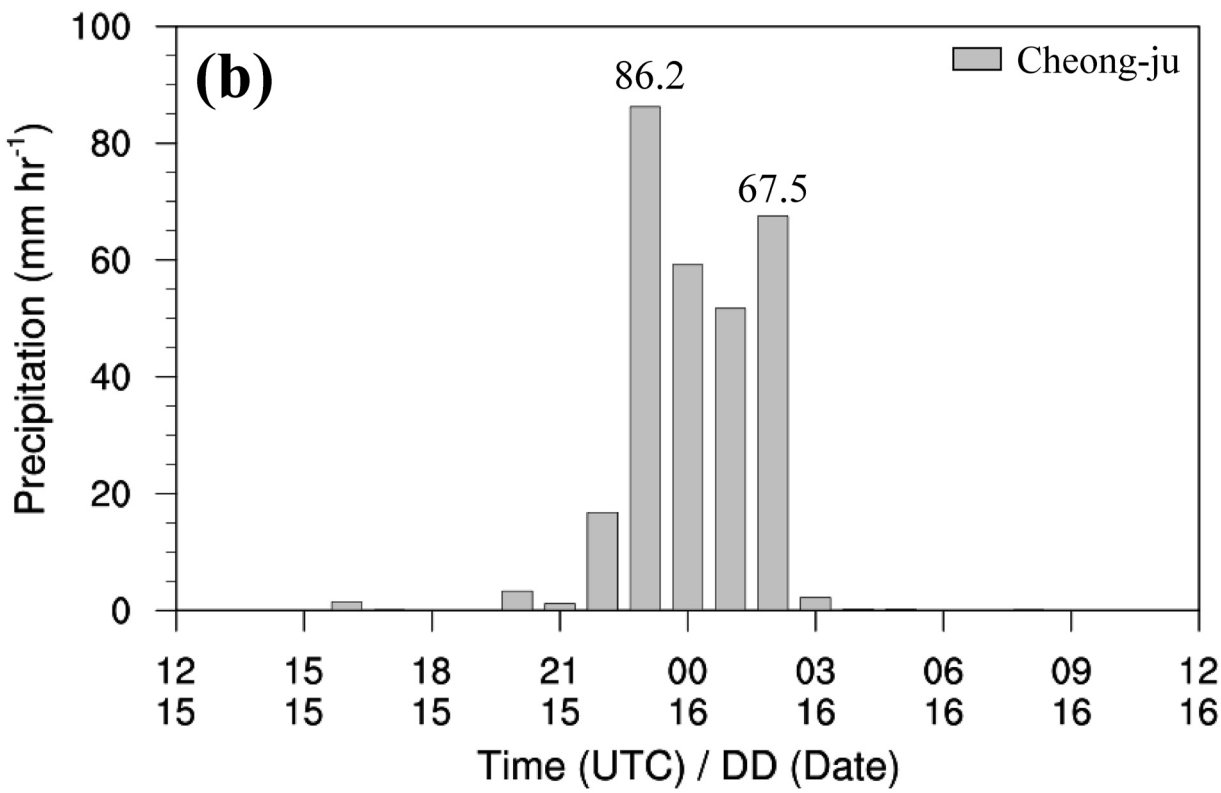

Figure 1. (a) Map of the study area showing the 24-hr accumulated rainfall amounts (mm) observed by automated surface observation systems (ASOS, black dots) and automatic weather stations (AWS, gray dots) in the central Korean Peninsula from 1200 UTC (2100 LST) on July 15, to 1200 UTC (2100 LST) on 16 July 2017 (The star mark denotes the location of Seoul and Cheong-ju), and (b) Bar plot of the time series of hourly rainfall from 1200 UTC (2100 LST) on July 15 to 1200 UTC (2100 LST) on 16 July 2017.

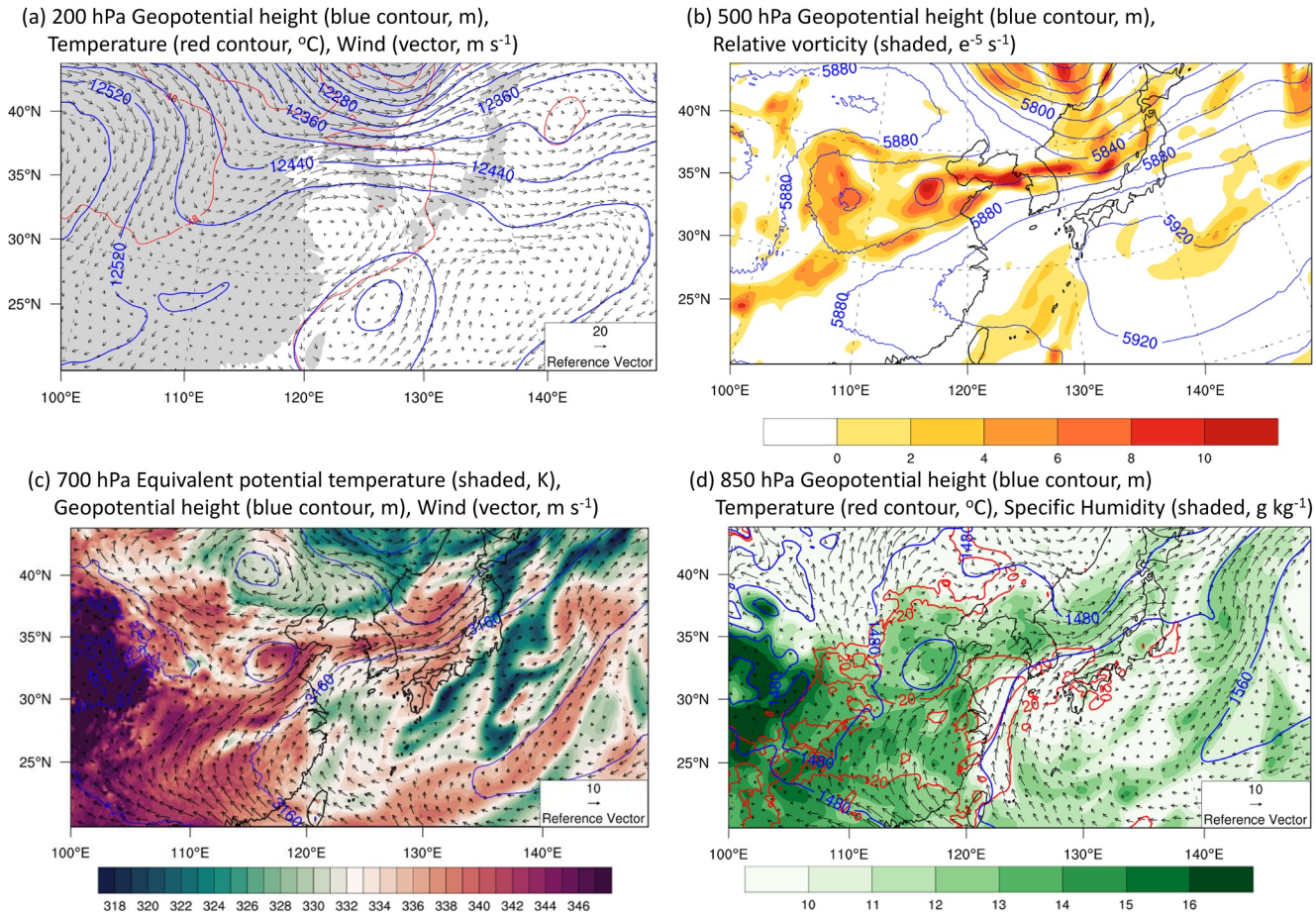

Figure 2. Spatial contour maps showing the synoptic fields from final analysis 0.25° reanalysis data at 1800 UTC on 15 July 2017.

with confluent flow, whereas warm and humid water vapor was transported into the central region of the Korean Peninsula. Figure 2c shows that the equivalent potential temperature (EPT) at 850 hPa is high. A positive relative vorticity was dominant over the central region of the Korean Peninsula, whereby the southwesterly wind enhanced the continuous moisture transport (Figure 2b). In addition, the divergence areas were consistent with the convergent flow areas of water vapor at the lower level (i.e., the Shandong Peninsula and Korean Peninsula), indicating that both dynamic and thermodynamic environments induced rising motion at the mid-level (see Figure S1 in Supporting Information S1). Environmental conditions, such as upper-level divergence, abundant water vapor supply, and significant atmospheric instability, are conducive to the development of a convection system. Figure 3 represents 3-hourly enhanced infrared (IR) satellite images obtained from 1600 UTC on July 15 to 0100 UTC on 16 July 2017. Two convective cells were present: a convective cell that originated off the coast of Gyeonggi-bay (hereafter referred to as CC1) and a deep-developed convective cell south of the Shandong Peninsula (hereafter called CC2). The CC1 generated in Gyeonggi-bay gradually developed and advanced to the southeast (Figures 3a and 3b). The CC2 developed in the south of the Shandong Peninsula and moved into the Yellow Sea over time. These cloud systems were the result of the rising motion and substantial low-level convergent areas accompanied by heavy rainfall.

2.2. Model Configuration and Experimental Design

The Advanced Research Weather Research and Forecasting (WRF) model (Skamarock et al., 2019) Version 4.1 was used in this study. The initial and boundary conditions were obtained from the 1° × 1° data of the National Centers for Environmental Prediction/National Centers for Atmospheric Research (NCEP/NCAR) FNL data. The simulation was performed for 72 hr. It was initialized at 0000 UTC on 14 July 2017, to provide a spin-up time

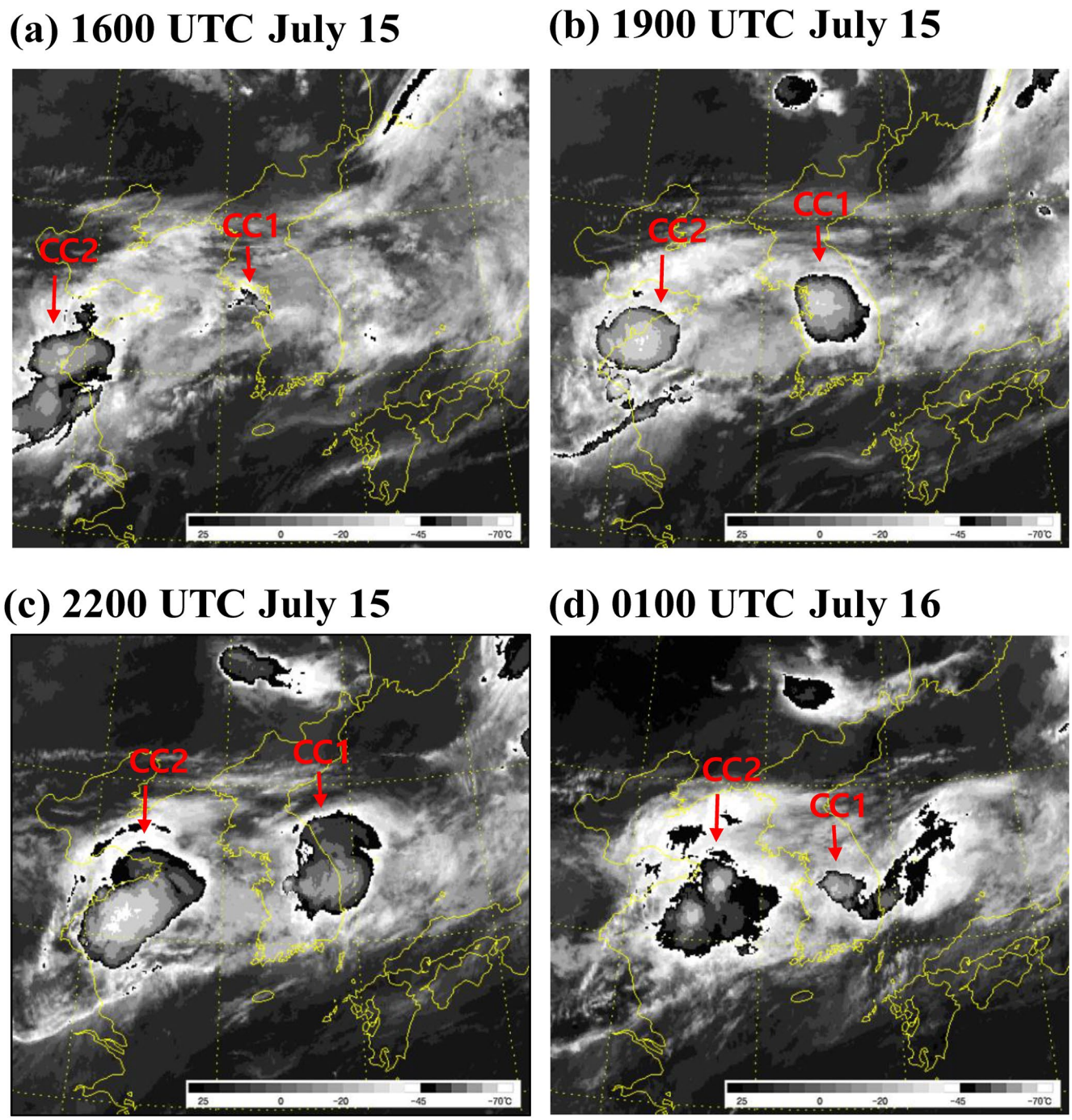

Figure 3. Three-hourly Enhanced IR satellite images showing cloud system development between 1600 UTC on July 15 and 0100 UTC on 16 July 2017.

of 36 hr before the occurrence of convection in the region. The model consisted of three domains with 36 km (201 × 201), 12 km (352 × 352), and 4 km (460 × 460) horizontal grid spacings, which included the CPS gray-zone resolution (Figure 4a). We used two-way nested domains with a Lambert conformal map projection. The domain contained 32 vertical levels from the surface to the top of the atmosphere at 50 hPa. The model used the WSM6 cloud microphysics scheme (Hong & Lim, 2006), Yonsei University planetary boundary layer scheme (Hong et al., 2006; Noh et al., 2003), Dudhia shortwave radiation scheme (Dudhia, 1989), and longwave radiation scheme based on the rapid radiative transfer model (Mlawer et al., 1997). In this study, the KF and MSKF schemes were employed for the sensitivity experiments.

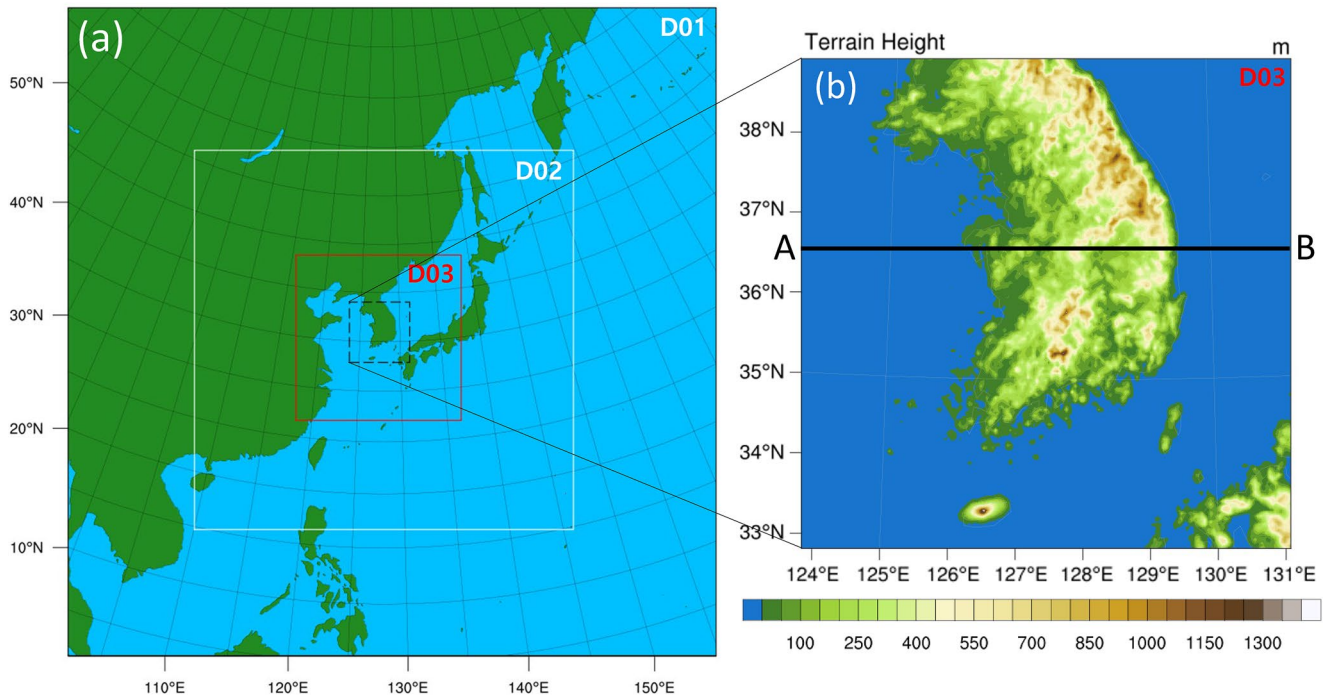

Figure 4. Map showing (a) Three nested domains with 36 km, 12 km, and 4 km grid spacings in Weather Research and Forecasting, and (b) terrain height for the finest domain (dashed box identified as the D03 domain in Figure 4a). Line AB in Figure 4b marks the vertical cross-section used in Figure 10.

The KF scheme is a subgrid scheme that simulates both deep and shallow convection using a mass flux approach to calculate the CAPE-based closure assumption scheme. The MSKF scheme is a scale-aware version of the KF scheme. Compared with the KF scheme, the MSKF scheme includes changes in the convective adjustment timescale and improvements of entrainment formulations (Zheng et al., 2016). The MSKF scheme also incorporates a grid-aware scaling parameter into these modifications. In addition, it includes cloud fraction adjustments (Alapaty, 2014; Alapaty et al., 2012) and an increased grid-scale velocity expressed in terms of the subgrid-scale updraft mass flux. In this study, we analyzed the two modifications (i.e., convective adjustment timescale and entrainment rate) affected by a grid-aware scaling parameter. The advantages of the two modifications of the MSKF are as follows:

Both the KF and MSKF schemes remove 90% of the CAPE within the convective timescale (Bechtold et al., 2001), which is limited to 1800 and 3600 s in the cloud layer for shallow and deep convections, respectively. The CAPE timescale (τ) is proportional to the grid length DX (Fritsch & Chappell, 1980; Fritsch et al., 1976). The CAPE timescale effectively removes the atmospheric instability at coarse grid resolution. However, a higher model grid resolution leads to an increase in the resolved cloud area and faster saturation speed, which causes rapid CAPE removal problems within the CAPE timescale, resulting in intense precipitation. To reduce these inadequacies, the MSKF scheme utilizes the adjustment timescale τ (s) based on Bechtold et al. (2008), which is multiplied by the scaling parameter (β) affected by the horizontal grid-scale (Zheng et al., 2016).

The CAPE adjustment timescale can be estimated as:

$$\tau = \frac{H}{(\delta m_b A_e)^{\frac{1}{3}}}\beta, \tag{1}$$

where H is the cloud depth (m), δm_b is the updraft mass flux of cloud base per unit density (m s^{-1}), A_e is the potential energy of the saturated air supplied to the cloud base (m^2 s^{-2}), and β is the scaling parameter defined as:

$$\beta = 1 + \ln\left(\frac{25}{DX}\right), \tag{2}$$

Table 1
List of Experiments Conducted in This Study

Experiments	Description
KF_D12	KF scheme used only for the D01 and D02 domains
KF	KF scheme used for all domains
MSKF	MSKF scheme used for all domains
CTS	Same as MSKF run, but for the same CAPE timescale as in KF scheme
ENT	Same as MSKF run, but for the same entrainment as in KF scheme

where β is ~2.8 at the 4-km model grid spacing in Equation 2, respectively. With the decrease in the grid spacing, the CAPE adjustment timescale using the scale-aware parameter increases. A longer CAPE timescale allows for the slower elimination of the convective instability.

In addition, the MSKF scheme adjusts the minimum entrainment rate using the scale-aware parameter, similar to the timescale concept. The adjusted entrainment rate is defined as:

$$\Delta M_e = M_b \frac{\alpha\beta}{z_{LCL}} \Delta p, \tag{3}$$

where M_b is the updraft mass flux per unit area (kg s^{-1}) at the cloud base, β is the scale-aware parameter [Equation 2], Δp is the pressure depth of a model level (Pa), and Z_{LCL} (m) is the height of the cloud base. The parameter α is a constant (0.03; Tokioka et al., 1988). The cloud base height replaces the arbitrarily fixed cloud radius because entrainment is associated with the subcloud layer depth. In general, the entrainment rate can change the convective process by determining the amount of mixing with the surrounding dry air. The increase in the entrainment rate prevents the occurrence of deep convections, especially in dry environments, as indicated by Lin et al. (2013). The higher horizontal resolution in Equation 3 enhances the entrainment process by increasing the scale-aware parameter (β). With the increase in the horizontal resolution (i.e., larger scale-aware parameter), the effects of the CPS are reduced by the enhanced entrainment, which inhibits deep convection. This adjusted scale-aware entrainment formulation allows the mixing rate, ΔM_e, to increase with the decreasing horizontal grid spacing. At higher resolutions, the effects of the KF scheme are reduced, which inhibits deep convection.

The investigations conducted in the present study consist of two parts. First, three experiments were conducted to investigate the difference between the KF and MSKF schemes and the effect of the CPS on the gray-zone (KF_D12, KF, and MSKF runs). The KF_D12 run employed the KF scheme only in the D01 and D02 domains with 36 and 12 km resolutions, respectively, whereas the KF and MSKF runs used both schemes in all domains. Subsequently, we conducted two additional experiments (CTS and ENT runs) to investigate the effects of the scale-aware parameter in the CAPE timescale and entrainment rate on the performance of the MSKF scheme for the simulation of the convective activity causing heavy rainfall. The CTS run was similar to the MSKF run, except that a scale-aware parameter value of 1 was employed for the CAPE timescale (i.e., the same CAPE timescale as in the KF scheme). The ENT run was similar to the MSKF scheme, but it employed the same entrainment rate as that used in the KF scheme. In the gray-zone (e.g., D03 domain), we examined the effects of the scale-aware parameter, that is, the CAPE timescale and entrainment rate, on the performance of the MSKF scheme based on comparing the CTS (ENT) and MSKF runs. The experiments conducted in this study are summarized in Table 1.

3. Results

3.1. Difference Between the KF and MSKF Schemes and the Effect of the CPS on the Gray-Zone

In this section, the precipitation simulations obtained from the KF_D12, KF, and MSKF runs are compared with the Integrated Multi-SatellitE Retrievals for Global Precipitation Measurement (IMERG, Huffman, Bolvin, Braithwaite, et al., 2015; Huffman, Bolvin, Nelkin, et al., 2015) and FNL 0.25° reanalysis data to analyze the rainfall and synoptic field differences among the three runs. Figure 5a shows two types of precipitation zones. One of the precipitation zones is that caused by CC1, which originated over the Seoul metropolitan region (Gyeonggi-bay) and moved in the southeastward direction. Another precipitation zone related to CC2 moved from the

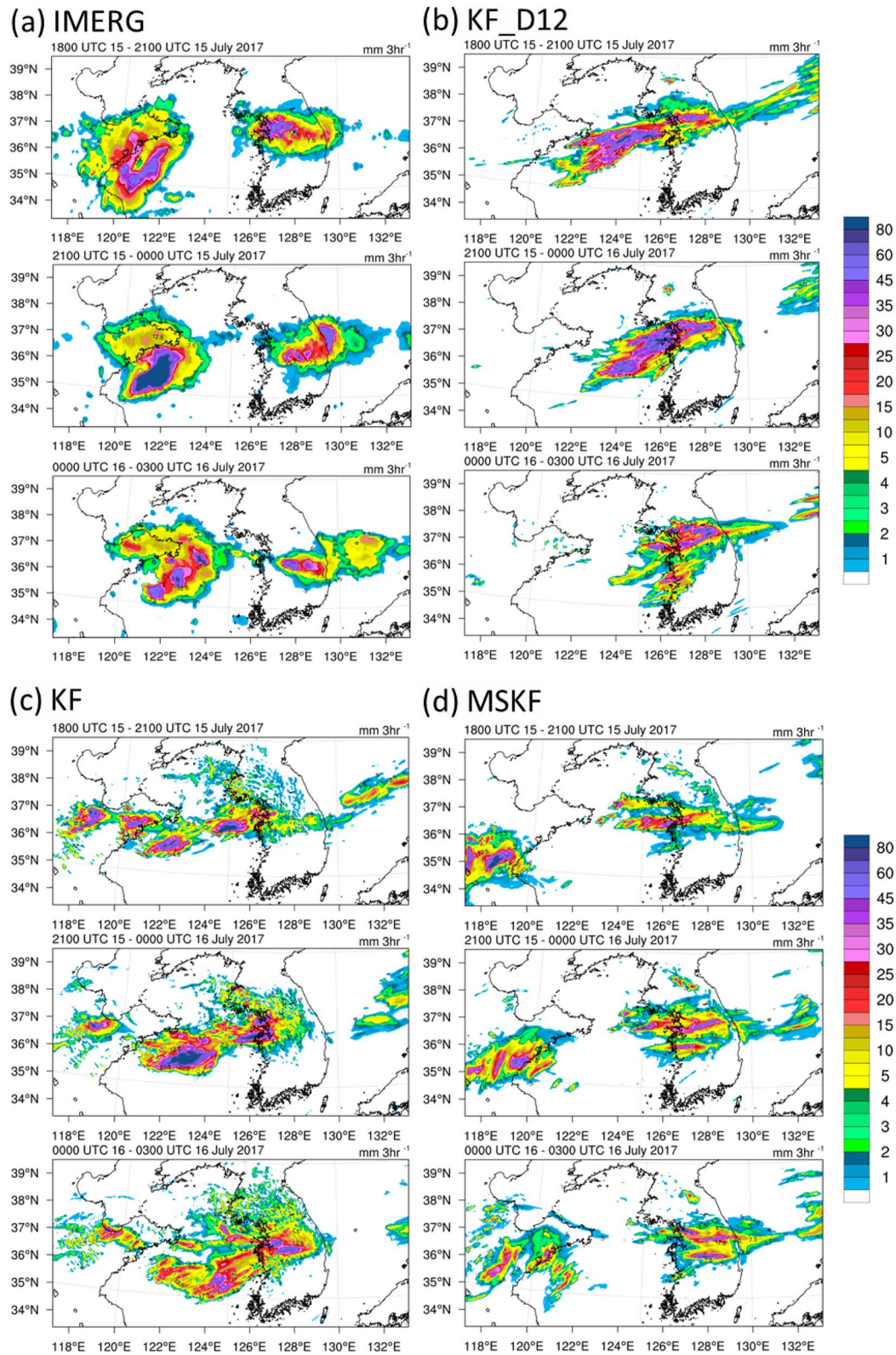

Figure 5. Spatiotemporal images showing three-hourly accumulated total precipitation (mm) in the D03 domain between 1800 UTC on July 15 and 0300 UTC on July 16.

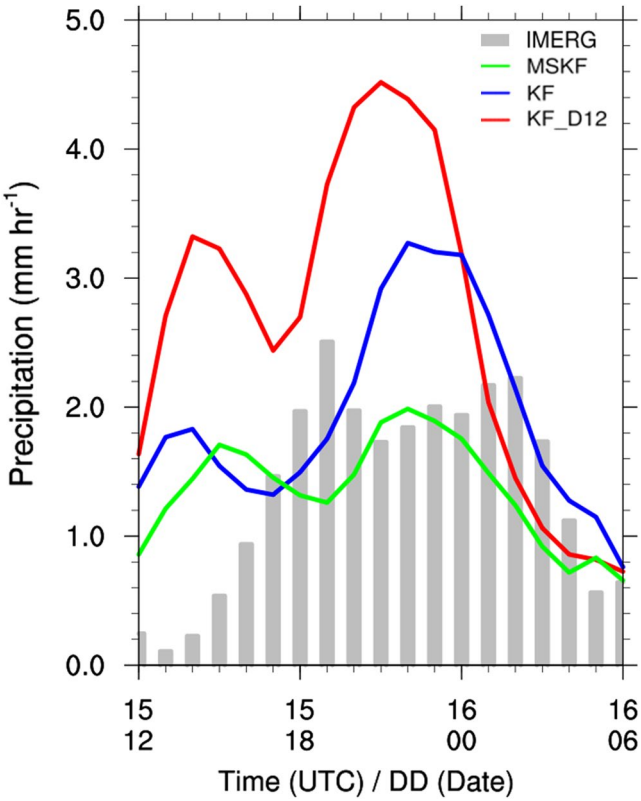

Figure 6. Graph depicting time-series of hourly accumulated rainfall averaged between 36 and 38°N and 123–130°E for the Integrated Multi-SatellitE Retrievals for Global Precipitation Measurement (IMERG) (gray box), KF_D12 (red line), KF (blue line), and Multiscale Kain–Fritsch (MSKF) (green line) run. Simulated precipitation is calculated from the results of the 4-km resolution domain.

Shandong Peninsula to the Yellow Sea. The IMERG satellite image indicates that the precipitation area related to CC1 over Gyeonggi-bay moved southeastward, resulting in heavy rainfall in Cheong-ju. Figures 5b–5d show the 3-hourly accumulated total (subgrid- and grid-scale) precipitation in the D03 domain for the three runs. In the KF_D12 run (Figure 5b), CC1 was located over the eastern part of Seoul and expanded northeastward; the model simulated only one convective system instead of two. Furthermore, the simulated precipitation associated with CC2 showed an unreasonable shift to the Yellow Sea instead of the southern part of the Shandong Peninsula, which caused an error; the rainfall in the ocean was overestimated. The KF run (Figure 5c) simulated features similar to those obtained from the KF_D12 run (i.e., overestimated precipitation over the Gyeonggi-bay). However, the precipitation core was shifted westward in the KF run compared with the KF_D12 run. In contrast, the MSKF run (Figure 5d) reproduced the spatial pattern of the simulated precipitation more accurately than the KF_D12 and KF runs. Note that CC1 and CC2 were separately simulated in the MSKF run, similar to the IMERG. Hence, the heavy rainfall related to CC1 was reasonably captured.

Figure 6 shows the time series of the domain-averaged hourly precipitation for observed (IMERG) and simulated precipitation (i.e., the D03 domain) averaged for the target region (between 36°N and 38°N and 123°E−130°E) including the Korean Peninsula and Yellow Sea. Heavy precipitation was observed for 18 hr (1200 UTC on July 15 to 0600 UTC on July 16), with two peaks at 1800 UTC on July 15 and 0300 UTC on July 16. However, based on the KF_D12 run, the two heavy precipitation peaks occurred earlier than in the observed conditions, with the overestimated precipitation caused by the unreasonable simulation in the Yellow Sea. The simulated precipitation of the KF run is more reasonable than that of the KF_D12 run. However, the precipitation in the target region was still overestimated compared with the IMERG. In contrast, the MSKF run more accurately simulated the heavy precipitation amount in the target region.

To quantitatively evaluate the performance of the heavy precipitation simulation (Figure 7), we calculated two standard skill scores (i.e., the treat score, TS, and bias score, BS) for precipitation with various intensity thresholds (e.g., 0.5, 5, 10, 20, 30, 40, and 50 mm). The two scores were computed from an interpolated precipitation simulation (i.e., the D03 domain) against IMERG estimated from 1200 UTC on July 15 to 0600 UTC on 16 July 2017, using Equations 4 and 5 (Wilks, 2011). As the BS and TS approach 1, the accuracy of the model forecast of rainfall events increases.

$$\mathrm{BS} = \frac{Hits + False\,alarms}{Hits + Misses},\ and \tag{4}$$

$$\mathrm{TS} = \frac{Hits}{Hits + False\,alarms + Misses}, \tag{5}$$

where "*Hits*" indicates the precipitation events that were simultaneously detected by the interpolated WRF model and IMERG an "*Miss*" (false alarm) represents the precipitation events detected by IMERG (i.e., the interpolated WRF model) but not by the interpolated WRF model (IMERG).

The precipitation detection skills (e.g., BS and TS) decreased with the increase in the threshold between the three runs (Figure 7). Compared with the other runs (e.g., the KF_D12 and KF runs), the TS of the precipitation forecast was the highest in the MSKF run for all precipitation thresholds. The BS results indicate that the KF and KF_D12 runs simulated more "false alarms" than "misses" compared with the MSKF run. Based on the BS of ~1, the MSKF run had a high model performance when detecting precipitation across the entire range of precipitation intensities. However, the BS of the KF and KF_D12 runs increased more significantly than that of the MSKF run. Notably, the BS of the KF_D12 run significantly increased with the increase in the threshold,

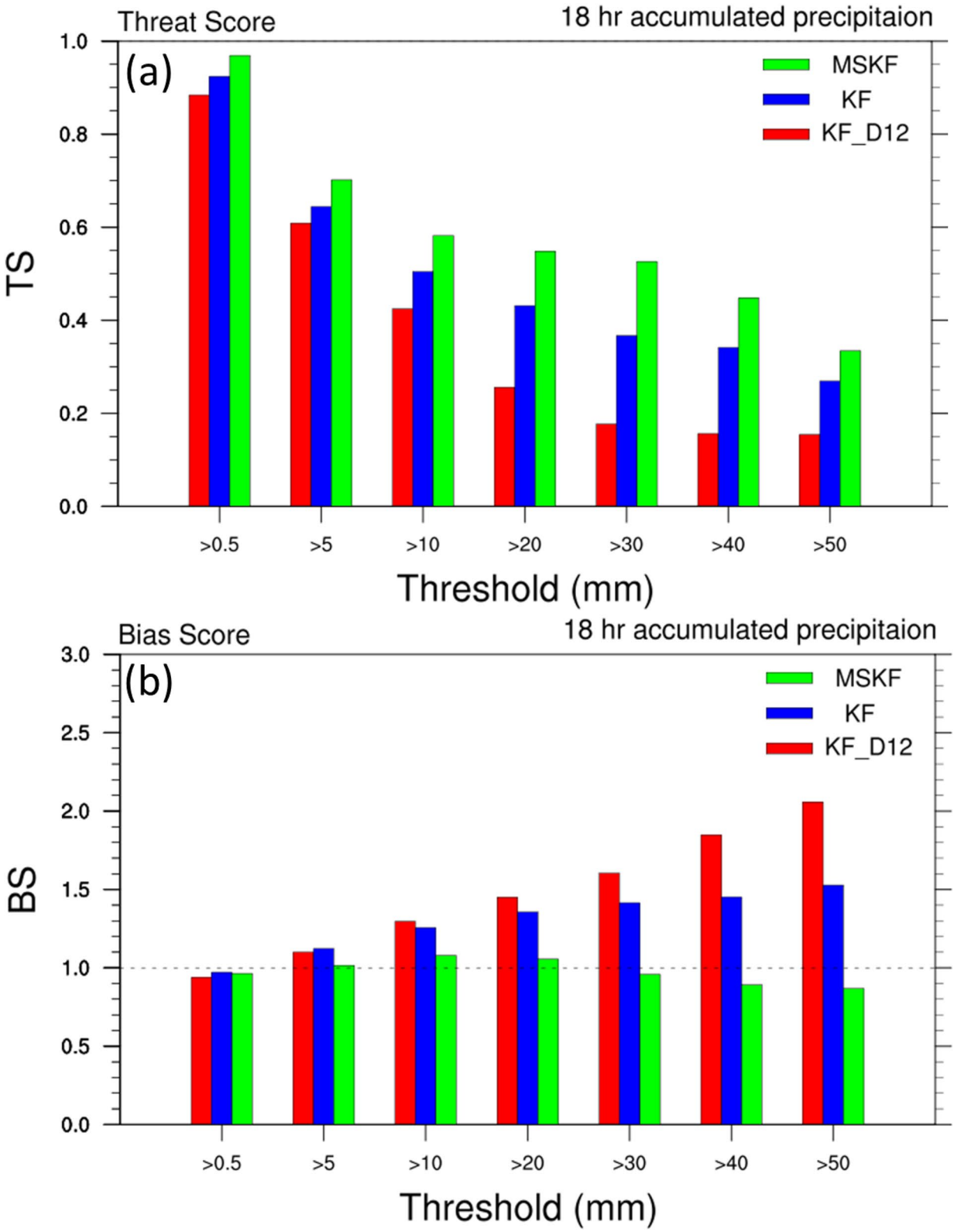

Figure 7. Bar plots of the statistical indices corresponding to the KF_D12, KF, and Multiscale Kain–Fritsch (MSKF) runs with Integrated Multi-SatellitE Retrievals for Global Precipitation Measurement based on different thresholds of 18-hourly accumulated precipitation (from 1200 UTC on July 15 to 0600 UTC on 16 July 2017). The simulated precipitation is interpolated to the observation grid points, and model statistics are calculated for South Korea and the Yellow Sea (between 36 and 38°N and 123–130°E). Simulated precipitation is calculated from the results of the 4-km resolution domain.

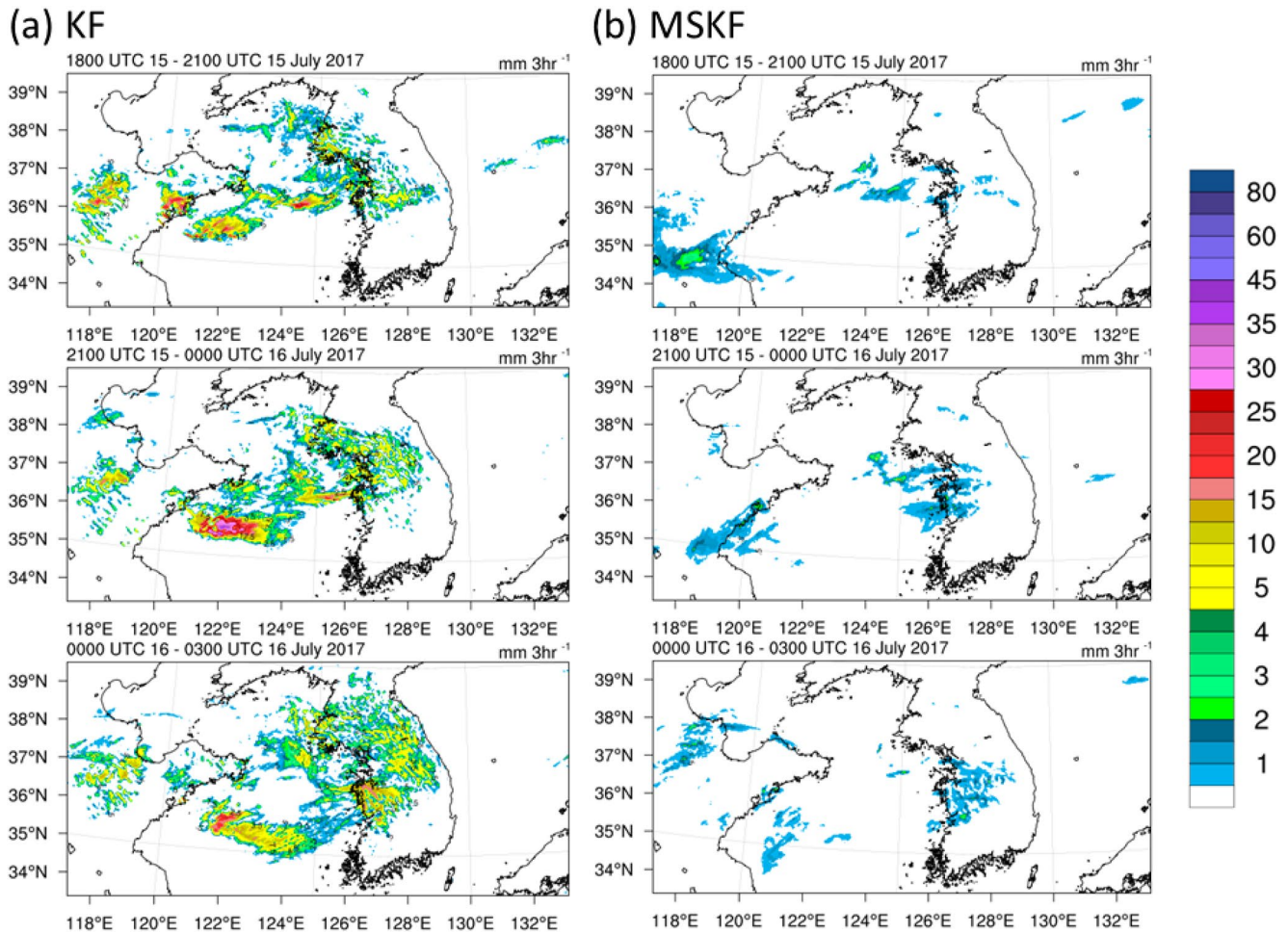

Figure 8. Spatiotemporal images (similar to Figure 5) for three-hourly accumulated subgrid-scale precipitation (mm).

suggesting that the number of "false alarms" or falsely classified grid boxes in the low-performance KF_D12 run is substantially larger than the number of "misses" or incorrectly classified grid boxes. The latter result means that, for each threshold, there were more grid boxes in which the KF_D12 run overestimated or incorrectly forecasted precipitation compared with the observed precipitation. The KF_D12 run contained many "false alarms" due to excessive precipitation in the Yellow Sea before entering the Korean Peninsula. In the KF and KF_D12 runs, the overall forecasting abilities of the precipitation products with respect to capturing the correct magnitude of intense precipitation are lower than that of the MSKF run.

Figure 8 shows the distribution of subgrid-scale precipitation simulated by the CPS. The subgrid-scale precipitation simulated by the KF run is similar to the KF_D12 run outside the D03 domain (i.e., in the D02 domain, not shown). However, within the D03 domain, only the KF run simulated subgrid-scale precipitation by employing the CPS for the domain. The KF_D12 run could not produce subgrid-scale precipitation due to the lack of the CPS in the D03 domain. In contrast, the subgrid-scale precipitation simulated in both of the D03 domains of the MSKF run was smaller compared with that in the KF run because the scale-aware parameter in the MSKF scheme decreases the role of CPS and increases the removal of atmospheric instabilities by the MPS.

To investigate the causes of the variations of the simulations among the three runs, we analyzed the synoptic conditions based on the reanalysis and simulations of the D03 domain (Figure 9). In the FNL (Figure 9a), low-level jets (LLJ >13 m s^{-1}) transporting wet and warm air were located in the two regions (e.g., the Shangdong and Korean Peninsulas) with heavy precipitation (Figure 5a). The three WRF runs reproduced wet and warm air transport by the LLJ from inland China to the Korean Peninsula. However, the LLJ cores were inappropriately located in inland China and the Yellow Sea in both the KF_D12 and KF runs (Figures 9b and 9c) and the intensity

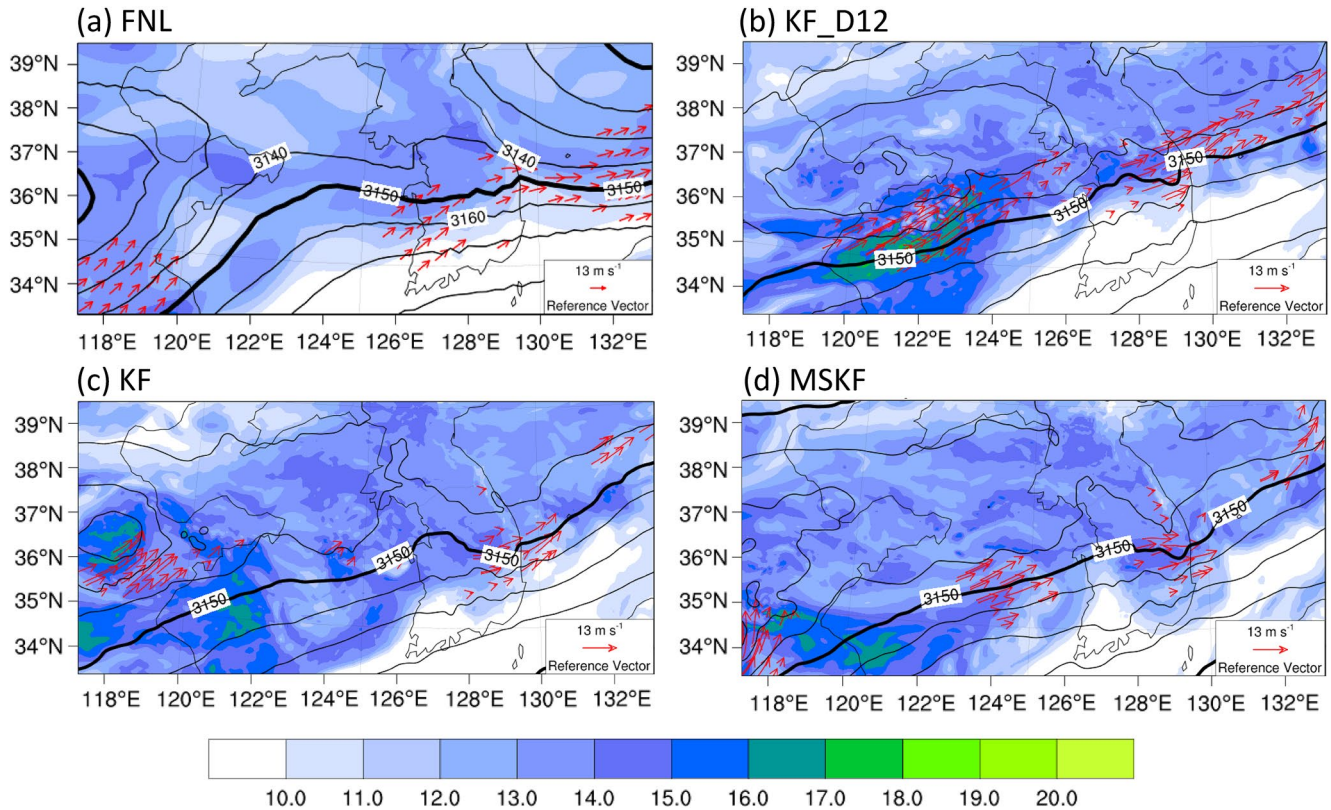

Figure 9. Spatial contour maps of the wind (>13 m s^{-1}, red vector) and water vapor (g kg^{-1}, shaded) at 850 hPa, and geopotential height (m, black lines) at 700 hPa in the D03 domain at 1800 UTC, 15 July 2017.

of the LLJ, which induced enhanced moisture transport, was overestimated. Note that LLJs located on the Shandong Peninsula in the reanalysis further shifted to the Yellow Sea in the KF_D12 run. In addition, low-pressure systems at 700 hPa developed in the LLJ cores in the KF_D12 and KF runs, which is unrealistic. Increased moisture transported by the enhanced LLJ led to increased convective instabilities over these regions in which convective activities and erroneous low-level pressure developed. In contrast, the location and intensity of the low-pressure system and LLJ were better simulated in the MSKF run than in the KF and KF_D12 runs.

The locations of the LLJ cores were consistent with those of the heavy precipitation areas of the three runs, implying that the LLJ played a significant role in the development of heavy precipitation by transporting wet and warm air from the subtropics. In the KF_D12 run in which the atmospheric instability was removed only by the MPS, grid-scale convection over the Yellow Sea was triggered relatively late. This led to an exaggerated atmospheric instability over the Yellow Sea, which was further enhanced by the distortion of synoptic fields (i.e., enhancing the LLJ and moisture convergence), as shown in Figure 9b, Figures S2a, and S2d in Supporting Information S1. In contrast, subgrid-scale precipitation on the Shandong Peninsula in the KF run implies that convection developed in the appropriate location. However, the action of the CPS was excessive, which led to the distortion of synoptic fields such as intensified LLJs and increased moisture convergence (Figures S2b and S2e in Supporting Information S1) on the Shandong Peninsula and in the Yellow Sea. The MPS also simulated considerable grid-scale precipitation in these regions, which is indicative of an unreasonable overestimation of the total precipitation by the CPS and MPS. However, in the MSKF run, the subgrid-scale precipitation decreased due to the decreasing role of the CPS compared with the KF run. The MSKF scheme appropriately triggered subgrid-scale convection over the Shandong Peninsula and the atmospheric instability was mainly removed by the MPS. Therefore, torrential rainfall over the Shandong Peninsula was reasonably captured in the MSKF run and the precipitation over the Yellow Sea was not overestimated.

These results imply that a high-resolution simulation of convective activities by the MPS alone can lead to an inappropriate overestimation of precipitation because the atmospheric instability may not be adequately reduced.

Furthermore, the CPS without scale-awareness may lead to an erroneous simulation of heavy precipitation at high resolution (Figure 8a and Figure S2b in Supporting Information S1) due to the exaggeration of convection and distortion of synoptic fields (Figure 9b and Figure S2e in Supporting Information S1). Therefore, the simulation of heavy precipitation using a high-resolution model might benefit from a scale-aware CPS.

3.2. Effects of Scale-Aware Parameters of the MSKF Scheme

In the previous section, we showed that the MSKF run improved the heavy precipitation simulation in the Cheong-ju region compared with the KF_D12 and KF runs. To investigate the reason for the improved simulation of heavy precipitation in the MSKF run, we conducted two additional sensitivity experiments for the scale-aware parameter of the MSKF scheme, that is, the CTS and ENT runs.

Figure 10 shows the simulated total precipitation, subgrid-scale precipitation, and synoptic fields reproduced by the D03 domain of the CTS and ENT runs. Figure 10a shows that the CTS run captured the heavy precipitation zones related to CC1 and CC2, similar to the MSKF run (see top panel of Figure 5d). However, when compared to the observed data, the simulated precipitation zone in the Yellow Sea caused by CC1 was shifted westward. In addition, compared with the MSKF run, the simulated subgrid-scale precipitation showed a marginal increase in the Yellow Sea (Figure 10b), suggesting that the reduced CAPE timescale of the CTS run compared with that of the MSKF run led to the faster removal of the atmospheric instability. The reduced CAPE timescale of the CTS run resulted in the rapid development of convective activity in the Yellow Sea rather than on the Korean Peninsula (Figure 10b), which unreasonably enhanced the moisture convergence and LLJ at 850 hPa (Figures 10c and 10d). Thus, based on the CTS run, the grid-scale precipitation in the Yellow Sea occurred earlier than in the MSKF run (Figure S3a in Supporting Information S1) and corresponding observation due to distorted synoptic conditions (Figure S3c in Supporting Information S1). In contrast, the ENT run (Figure 10e) simulated an unrealistic merged precipitation zone in the Yellow Sea, similar to the KF run (Figure 5c). Compared with the CTS and MSKF runs, the ENT run overestimated subgrid-scale precipitation in the Yellow Sea because the entrainment rate was relatively weak due to the absence of scale-aware parameters (Figure 10f). Therefore, the ENT run simulated the enhanced convective activity and excessive subgrid-scale precipitation in the Yellow Sea based on the CPS (Figure S3b in Supporting Information S1). Furthermore, enhanced convective activities led to the distortion of synoptic fields such as the intensified LLJ and exaggerated moisture convergence, which caused excessive grid-scale precipitation in the Yellow Sea (Figure 10g and 10h, Figure S3b, and S3d in Supporting Information S1). Therefore, the MSKF run more accurately simulated heavy precipitation compared with the KF and KF_D12 runs because of the increased CAPE timescale and enhanced entrainment, which led to a better modulation of the atmospheric instability. In other words, the subgrid-scale (grid-scale) precipitation by the CPS (MPS) smoothly decreased (increased) in the MSKF run with the increase in the horizontal resolution in the gray-zone. The precipitation error of the ENT run is more significant than that of the CTS run, indicating that the enhanced entrainment rate of the MSKF scheme contributed more to the improved simulation of heavy precipitation than the increased CAPE timescale.

To investigate the effects of scale-aware parameters on convection development, we examined the vertical fields across the region in which the difference in the precipitation was prominent between the sensitivity runs (Figures 11 and 12; see solid line in Figure 4b). The analysis times were 1800 and 2100 UTC on July 15, which were appropriate to examine the effects of the scale-aware parameter. Figure 11 shows a notable difference in the vertical distribution of the EPT compared with those of the other experiments in the Yellow Sea (123.6°E) and Cheong-ju region (127.9°E). The CTS run simulated a high EPT at the low level in the Yellow Sea, which increased the atmospheric instability, followed by the development of unreasonably intense convective activity between 124.5°E−125.5°E (Figures 11a and 11d). As shown in Figures 10e and 11g, the shorter CAPE timescale in the CTS run than in the MSKF run triggered convection earlier in the Yellow Sea rather than on the west coast of the Korean Peninsula. The earlier development of convection in the Yellow Sea enhanced the LLJ and moisture convergence, which explains the excessive grid-scale precipitation (Figures 12a and 12d). In addition, convection in the inland of the Korean Peninsula was not simulated; hence, the torrential precipitation in Cheong-ju was not accurately captured (see Figure 10a). Similarly, the ENT run also simulated a high EPT at low levels (Figures 11b and 11e). The entrainment was weaker in the ENT run due to the absence of a scale-aware entrainment parameter. Because the entrainment of cooler and drier environmental air weakens deep moist convection, the weaker entrainment in the ENT run led to precipitation overestimation in the Yellow Sea, as shown in Figure 10e. The

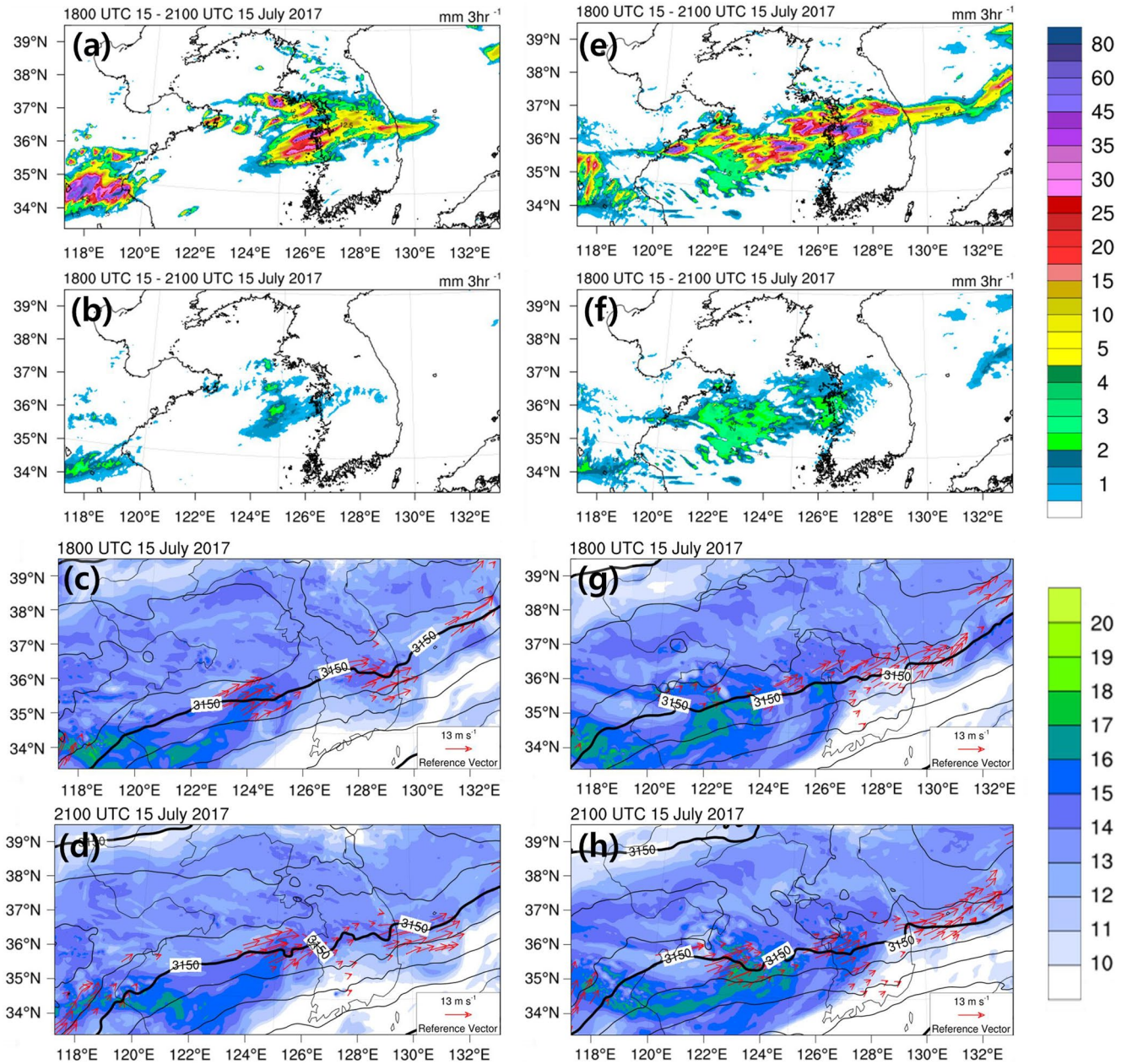

Figure 10. Spatial maps of the (a and e) total precipitation (mm) and (b and f) subgird-scale precipitation (mm) between 1800 and 2100 UTC, 15 July 2017, and 850 hPa wind (m s^{-1}, red vector) and water vapor (g kg^{-1}, shaded), and 700 hPa geopotential height (m, black lines) at (c,g) 1800 UTC and (d,h) 2100 UTC, 15 July 2017 at the D03 domains of the CTS and ENT runs.

misplaced LLJ and water vapor convergence also contributed to overestimated precipitation in the Yellow Sea region. Because most of the precipitation occurred in the Yellow Sea in the ENT run, the inland precipitation of the Korean Peninsula was considerably underestimated (Figure 10e). On the other hand, the MSKF run reproduced strong convection and precipitation over the Cheong-ju region (127.9°E), which resulted in the reasonable simulation of heavy precipitation by the CPS and MPS. This implies that the low-level EPT, atmospheric stability, and hydrometeors over the Yellow Sea obtained with the MSKF run are more realistic (Figures 11c, 11f, 12c, and 12f).

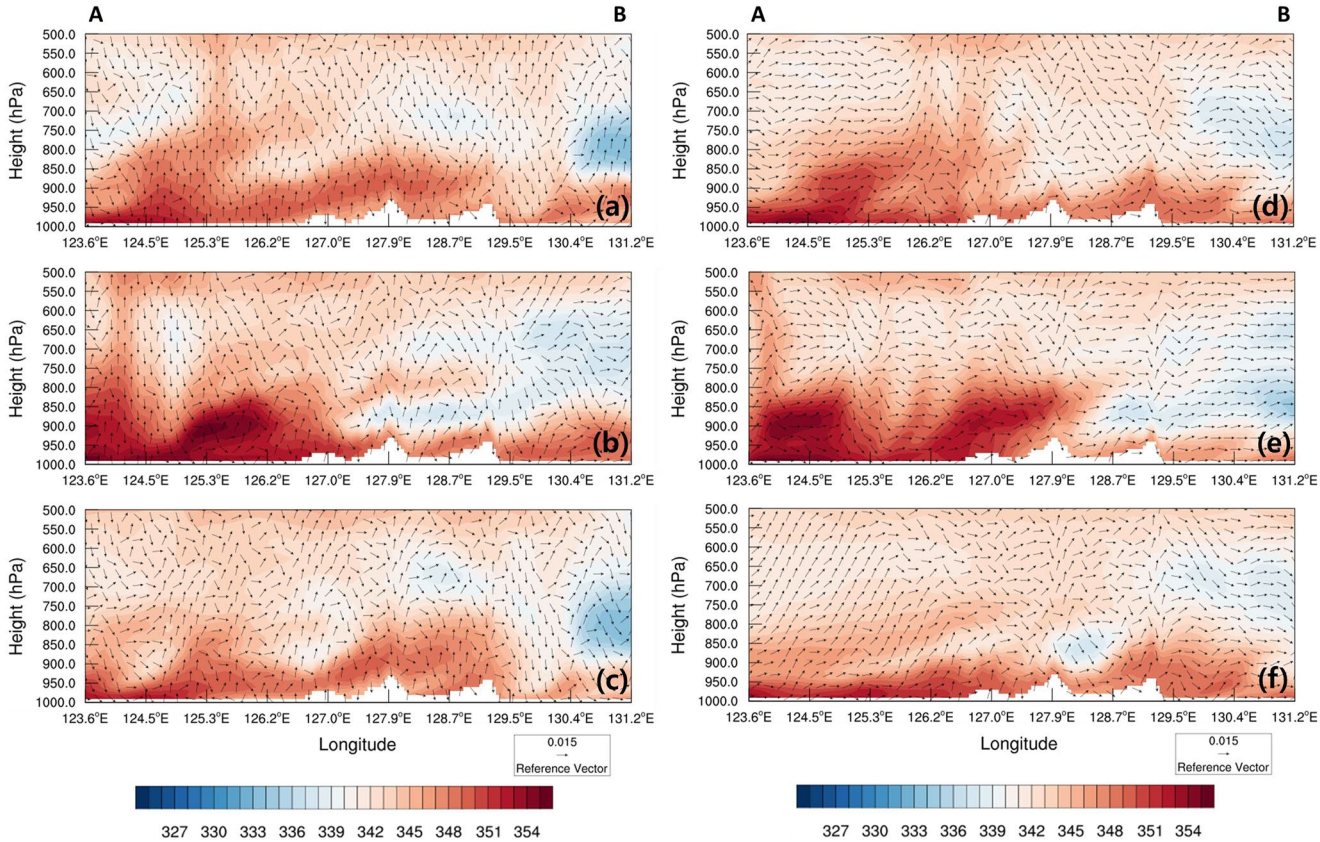

Figure 11. Plots of the vertical cross-sections (AB in Figure 4b) of equivalent potential temperature (K, shaded) and wind (m s^{-1}, vector) at (a–c) 1800 UTC and (d–f) 2100 UTC, 15 July 2017 in the D03 domain. Upper, middle, and lower panels indicate the CTS, ENT, and Multiscale Kain–Fritsch runs, respectively.

4. Conclusion

In this study, the effect of a scale-aware CPS on the gray-zone in the WRF model of a heavy precipitation event over the Korean Peninsula was investigated. We selected the KF and MSKF schemes as non-scale- and scale-aware CPSs, respectively. The MSKF scheme uses a scale-aware parameter modifying the CAPE timescale and entrainment process of the KF scheme as a function of the horizontal grid spacing. The multi-nesting method was employed with three domains with 36, 12, and 4 km horizontal resolutions to consider the gray-zone resolution.

Based on our results, the KF runs (i.e., the KF_D12 and KF runs) overestimated the precipitation in the Yellow Sea and distorted synoptic fields such as the LLJs and moisture convergence. In the KF_D12 run, only the MPS resolved the convective activities for the domain with high resolution (i.e., 4 km) and overestimated the grid-scale precipitation in the Yellow Sea because the atmospheric instability was inadequately reduced. The CPS without scale-awareness (i.e., KF run) also caused erroneous precipitation simulations due to the exaggeration of convection and distortion of synoptic fields. In contrast, the precipitation and synoptic fields were realistically simulated in the MSKF run. Our sensitivity experiments for the MSKF scale-aware parameters (i.e., the CTS and ENT runs) showed that the shorter CAPE timescale and decreased entrainment process of the KF scheme compared with those of the MSKF scheme led to the unreasonable, rapid development and exaggeration of the convective activity, respectively. In addition, the simulated precipitation error of the ENT run was more significant than that of the CTS run, suggesting that the enhanced entrainment process of the MSKF scheme contributed more to the improved simulation of heavy precipitation than the increased CAPE timescale. Consequently, the precipitation and synoptic fields were realistically simulated with the MSKF scheme including a scale-aware parameter based on the decrease in the subgrid-scale convection via the CPS and the increase in the grid-scale convection by MPS with the increase in the horizontal resolution.

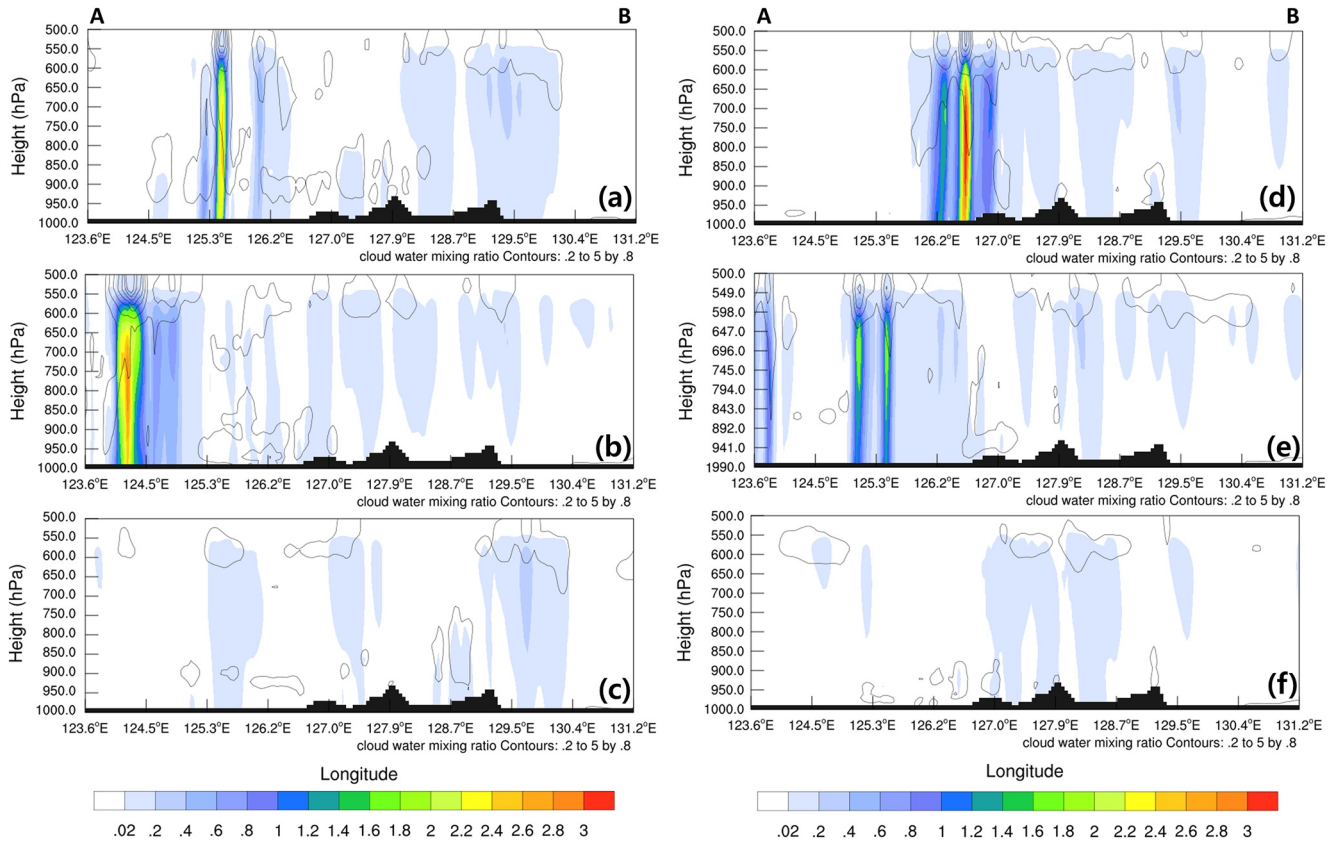

Figure 12. As in Figure 11, but for cloud hydrometeors mixing ratio (g kg^{-1}, shaded) and rain water mixing ratio (g kg^{-1}, contour). Cloud hydrometeors are calculated by the summation of cloud water, ice, snow, and graupel.

More realistic grid-scale simulations are required because the horizontal resolution of numerical weather forecasting models has increased due to computing resource advances. The results of studies showed that scale-aware physics schemes can improve the high-impact weather simulation of high-resolution (e.g., ~3 km) numerical models (Hong & Dudhia, 2012; Jeworrek et al., 2019). The results of our study provide insights into the role of the scale-aware CPS in the simulation of heavy precipitation at high resolutions (e.g., ~4 km). However, our study has limitations. Only KF-based CPSs of the WRF model and a heavy rainfall case in the Korean Peninsula were tested. Further studies should be carried out to investigate the application of various scale-aware CPSs (e.g., scale-aware Grell-Freitas; Grell & Freitas, 2014) and Simplified Arakawa–Schubert schemes for the gray-zone (Kwon & Hong, 2017) to heavier precipitation events. In addition, sensitivity tests should be conducted with various combinations of scale-aware CPSs and MPSs because the predictability of convective systems associated with heavy rainfall depends on these combinations. However, our results are encouraging and highlight the potential of scale-aware convective parameterizations for improving rainfall and synoptic-scale meteorology at various resolutions.

Data Availability Statement

The National Centers for Environmental Prediction Global Final Analysis (NCEP-FNL) data are available online (https://rda.ucar.edu/datasets/ds083.2/ and https://rda.ucar.edu/datasets/ds083.3/). The IMERG data were provided by the NASA Goddard Space Flight Center's IMERG and PPS teams, which develop and compute IMERG as a contribution to the GPM mission. They are archived at the NASA GES DISC (https://disc.gsfc.nasa.gov/datasets/GPM_3IMERGHH_V06/summary) and online (https://gpm.nasa.gov/data/directory). The WRF model used in this study can be found in online repositories. The WRF model Version 4.1, which was developed on 13 April 2019, can be accessed online (https://github.com/wrf-model/WRF/tree/release-v4.1). The WRF simulation data can be accessed on the GitHub repository (https://doi.org/10.5281/zenodo.6459839).

Acknowledgments
This work was funded by the Korea Meteorological Administration Research and Development Program under Grant KMI(KMI2020-01214).

References

Alapaty, K. (2014). Multiscale Kain-Fritsch scheme: Formulations and tests. In *Paper presented at 13th Annual CMAS Conference*.

Alapaty, K., Herwehe, J. A., Otte, T. L., Nolte, C. G., Bullock, O. R., Mallard, M. S., et al. (2012). Introducing subgrid-scale cloud feedbacks to radiation for regional meteorological and climate modeling. *Geophysical Research Letters*, *39*(24), 2012GL054031. https://doi.org/10.1029/2012GL054031

Arakawa, A., Jung, J. H., & Wu, C. M. (2011). Toward unification of the multiscale modeling of the atmosphere. *Atmospheric Chemistry and Physics*, *11*(8), 3731–3742. https://doi.org/10.5194/acp-11-3731-2011

Arakawa, A., Jung, J.-H., & Wu, C.-M. (2016). Multiscale modeling of the moist-convective atmosphere. *Meteorological Monographs*, *56*, 16–17. https://doi.org/10.1175/AMSMONOGRAPHS-D-15-0014.1

Bechtold, P., Bazile, E., Guichard, F., Mascart, P., & Richard, E. (2001). A mass-flux convection scheme for regional and global models. *Quarterly Journal of the Royal Meteorological Society*, *127*(573), 869–886. https://doi.org/10.1002/qj.49712757309

Bechtold, P., Koehler, M., Jung, T., Doblas-Reyes, F., Leutbecher, M., Rodwell, M. J., et al. (2008). Advances in simulating atmospheric variability with the ECMWF model: From synoptic to decadal time-scales. *Applied Meteorology, and Oceanography*, *134*(634), 1337–1351. https://doi.org/10.1002/qj.289

Bechtold, P., Semane, N., Lopez, P., Chaboureau, J.-P., Beljaars, A., & Bormann, N. J. (2014). Representing equilibrium and non equilibrium convection in large-scale models. *Journal of the Atmospheric Sciences*, *71*(2), 734–753. https://doi.org/10.1175/jas-d-13-0163.1

Bengtsson, L., & Körnich, H. (2016). Impact of a stochastic parametrization of cumulus convection, using cellular automata. *A mesoscale ensemble prediction system*, *142*(695), 1150–1159. https://doi.org/10.1002/qj.2720

Bryan, G. H., Wyngaard, J. C., & Fritsch, J. M. (2003). Resolution requirements for the simulation of deep moist convection. *Monthly Weather Review*, *131*(10), 2394–2416. https://doi.org/10.1175/1520-0493(2003)131<2394:rrftso>2.0.co;2

Charles, M. E., Colle, B. A. J. W., & forecasting. (2009). Verification of extratropical cyclones within the NCEP operational models. Part I: Analysis errors and short-term NAM and GFS forecasts. *Weather and Forecasting*, *24*(5), 1173–1190. https://doi.org/10.1175/2009waf2222169.1

Cho, N.-S., & Lee, T.-Y. (2006). A numerical study of multiple convection bands over the Korean peninsula. *Asia-Pacific Journal of Atmospheric Sciences*, *42*(2), 87–105.

Choi, G., Kwon, W.-T., Boo, K.-O., & Cha, Y.-M. J. 대. (2008). Recent spatial and temporal changes in means and extreme events of temperature and precipitation across the Republic of Korea. *Journal of the Korean Geographical Society*, *43*(5), 681–700.

Choi, Y., Lee, H., & Kwon, J. (2013). Recent change on frequency-magnitude of summer extreme rainfall events over the Republic of Korea. *The geographical journal of Korea*, *47*(1), 83–97.

Davies, T., Cullen, M. J., Malcolm, A. J., Mawson, M., Staniforth, A., White, A., & Wood, N. (2005). A new dynamical core for the Met Office's global and regional modelling of the atmosphere. *Applied Meteorology, and Oceanography*, *131*(608), 1759–1782. https://doi.org/10.1256/qj.04.101

Deng, A., Stauffer, D. R. J., & climatology. (2006). On improving 4-km mesoscale model simulations. *Journal of Applied Meteorology and Climatology*, *45*(3), 361–381. https://doi.org/10.1175/jam2341.1

Dudhia, J. (1989). Numerical study of convection observed during the winter monsoon experiment using a mesoscale two-dimensional model. *Journal of the Atmospheric Sciences*, *46*(20), 3077–3107. https://doi.org/10.1175/1520-0469(1989)046<3077:nsocod>2.0.co;2

Freitas, S. R., Grell, G. A., Molod, A., Thompson, M. A., Putman, W. M., Santos e Silva, C. M., & Souza, E. P. (2018). Assessing the Grell-Freitas convection parameterization in the NASA GEOS modeling system, *10*(6), 1266–1289, https://doi.org/10.1029/2017MS001251

Fritsch, J. M., & Chappell, C. F. (1980). Numerical prediction of convectively Driven mesoscale pressure systems. Part I: Convective parameterization. *Journal of the Atmospheric Sciences*, *372*(8), 1722–1733. https://doi.org/10.1175/1520-0469(1980)037<1722:Npocdm>2.0.Co

Fritsch, M. J., Chappell, C. F., & Hoxit, L. R. (1976). The use of large-scale budgets for convective parameterization. *Monthly Weather Review*, *1042*(11), 1408–1418. https://doi.org/10.1175/1520-0493

Gerard, L., Piriou, J.-M., Brožková, R., Geleyn, J.-F., & Banciu, D. J. (2009). Cloud and precipitation parameterization in a meso-gamma-scale operational weather prediction model. *Monthly Weather Review*, *137*(11), 3960–3977. https://doi.org/10.1175/2009mwr2750.1

Grell, G. A., & Freitas, S. (2014). A scale and aerosol aware stochastic convective parameterization for weather and air quality modeling. *Atmospheric Chemistry*, *14*(10), 5233–5250. https://doi.org/10.5194/acp-14-5233-2014

Gustafson, J. W. I., Ma, P. L., Xiao, H., Singh, B., Rasch, P. J., & Fast, J. (2013). The Separate Physics and Dynamics Experiment (SPADE) framework for determining resolution awareness. *A case study of microphysics*, *118*(16), 9258–9276. https://doi.org/10.1002/jgrd.50711

Ha, K.-J., Park, S.-K., & Kim, K.-Y. (2005). On interannual characteristics of Climate Prediction Center merged analysis precipitation over the Korean Peninsula during the summer monsoon season. *International Journal of Climatology*, *25*(1), 99–116. https://doi.org/10.1002/joc.1116

Han, J., Pan, H.-L., & Forecasting. (2011). Revision of convection and vertical diffusion schemes in the NCEP Global Forecast System. *Weather and Forecasting*, *26*(4), 520–533. https://doi.org/10.1175/waf-d-10-05038.1

Han, J.-Y., & Hong, S.-Y. (2018). Precipitation Forecast experiments using the weather research and Forecasting (WRF) model at gray-zone resolutions. *Weather and Forecasting*, *33*(6), 1605–1616. https://doi.org/10.1175/waf-d-18-0026.1

Ho, C.-H., & Kang, I.-S. J. J. K. M. S. (1988). The variability of precipitation in Korea. *International Journal of Climatology*, *24*(1), 38–48.

Ho, C.-H., Lee, J. Y., Ahn, M. H., & Lee, H. S. (2003). A sudden change in summer rainfall characteristics in Korea during the late 1970s. *International Journal of Climatology*, *23*(1), 117–128. https://doi.org/10.1002/joc.864

Hong, S.-Y., & Dudhia, J. (2012). Next-generation numerical weather prediction: Bridging parameterization, explicit clouds, and large eddies. *Bulletin of the American Meteorological Society*, *93*(1), ES6–ES9. https://doi.org/10.1175/2011bams3224.1

Hong, S.-Y., & Lee, J.-W. J. A. R. (2009). Assessment of the WRF model in reproducing a flash-flood heavy rainfall event over Korea. *Atmospheric Research*, *93*(4), 818–831. https://doi.org/10.1016/j.atmosres.2009.03.015

Hong, S.-Y., & Lim, J.-O. (2006). The WRF single-moment 6-class microphysics scheme (WSM6). *Asia-Pacific Journal of Atmospheric Sciences*, *42*(2), 129–151.

Hong, S.-Y., Noh, Y., & Dudhia, J. (2006). A new vertical diffusion package with an explicit treatment of entrainment processes. *Monthly Weather Review*, *134*(9), 2318–2341. https://doi.org/10.1175/mwr3199.1

Huffman, G. J., Bolvin, D. T., Braithwaite, D., Hsu, K., Joyce, R., Xie, P., & Yoo, S.-H. (2015). NASA global precipitation measurement (GPM) integrated multi-satellite retrievals for. GPM (IMERG). *Algorithm Theoretical Basis Document (ATBD) Version, 4*, 26

Huffman, G. J., Bolvin, D. T., Nelkin, E. J., & Tan, J. J. N. G. C. (2015). Integrated Multi-satellitE Retrievals for GPM (IMERG) technical documentation. *NASA/GSFC Code*, *612*(47), 2019

Jankov, I., Schultz, P. J., Anderson, C. J., & Koch, S. E. (2007). The impact of different physical parameterizations and their interactions on cold season QPF in the American River basin. *Journal of Hydrometeorology*, *8*(5), 1141–1151. https://doi.org/10.1175/jhm630.1

Jee, J.-B., & Kim, S. J. A. (2017). Sensitivity study on high-resolution WRF precipitation forecast for a heavy rainfall event. *Atmosphere*, *8*(6), 96. https://doi.org/10.3390/atmos8060096

Jeworrek, J., West, G., & Stull, R. (2019). Evaluation of cumulus and microphysics parameterizations in WRF across the convective gray zone. *Weather and Forecasting*, *34*(4), 1097–1115. https://doi.org/10.1175/waf-d-18-0178.1

Kain, J. S. (2004). The Kain–Fritsch convective parameterization: An update. *Journal Of Applied Meteorology*, *43*(1), 170–181. https://doi.org/10.1175/1520-0450(2004)043<0170:tkcpau>2.0.co;2

Kang, I.-S., Ho, C.-H., & Min, K.-D. (1992). Long-range forecast of summer precipitation in Korea. *Journal of Korean Meteorological Society*, *28*(3), 283–292.

Khairoutdinov, M., & Randall, D. (2006). High-resolution simulation of shallow-to-deep convection transition over land. *Journal of the Atmospheric Sciences*, *63*(12), 3421–3436. https://doi.org/10.1175/jas3810.1

Kim, C., Seo, M.-S., & Atmosphere, k. J. (2008). Change-point in the recent. Precipitation over South Korea. *Atmosphere*, *18*(2), 113–122.

Kim, C., & Suh, M.-S. J. A. (2008). Change-point in the recent (1976-2005) precipitation over South Korea, *18*(2), 111–120.

Kuang, Z., & Bretherton, C. (2006). A mass-flux scheme view of a high-resolution simulation of a transition from shallow to deep cumulus convection, *63*(7), 1895–1909, https://doi.org/10.1175/jas3723.1

Kwon, M., Jhun, J.-G., & Ha, K.-J. (2007). Decadal change in East Asian summer monsoon circulation in the mid-1990s. *Geophysical Research Letters*, *34*(21), L21706. https://doi.org/10.1029/2007GL031977

Kwon, Y. C., & Hong, S.-Y. (2017). A mass-Flux cumulus parameterization scheme across gray-zone resolutions. *Monthly Weather Review*, *145*(2), 583–598. https://doi.org/10.1175/mwr-d-16-0034.1

Lee, J.-Y., Kwon, M., Yun, K.-S., Min, S.-K., Park, I.-H., Ham, Y.-G., et al. (2017). The long-term variability of Changma in the East Asian summer monsoon system: A review and revisit, *53*(2), 257–272, https://doi.org/10.1007/s13143-017-0032-5

Lee, S.-H., Kim, E.-K., & Heo, I.-H. (2011). A study on variability of extreme precipitation by basin in South Korea, *17*(5), 505–520.

Lee, S.-W., Lee, D.-K., & Chang, D.-E. (2011). Impact of horizontal resolution and cumulus parameterization scheme on the simulation of heavy rainfall events over the Korean Peninsula. *Advances in Atmospheric Sciences*, *28*(1), 1–15. https://doi.org/10.1007/s00376-010-9217-x

Lee, T.-Y., & Kim, Y.-H. (2007). Heavy precipitation systems over the Korean peninsula and their Classification. *Asia-Pacific Journal of the Atmospheric Sciences*, *43*, 367–396.

Liang, X. Z., Li, Q., Mei, H., & Zeng, M. (2019). Multi-grid nesting ability to represent convections across the gray zone. *Journal of Advances in Modeling Earth Systems*, *11*(12), 4352–4376. https://doi.org/10.1029/2019ms001741

Lin, C., & Arakawa, A. (1997). The macroscopic entrainment processes of simulated cumulus ensemble. Part I: Entrainment sources. *Journal of the atmospheric sciences*, *54*(8), 1027–1043. https://doi.org/10.1175/1520-0469(1997)054<1027:tmepos>2.0.co;2

Lin, Y., Zhao, M., Ming, Y., Golaz, J.-C., Donner, L. J., Klein, S. A., et al. (2013). Precipitation partitioning, tropical clouds, and intraseasonal variability in GFDL AM2. *Journal of Climate*, *26*(15), 5453–5466. https://doi.org/10.1175/jcli-d-12-00442.1

Lowrey, M. R. K., & Yang, Z.-L. (2008). Assessing the capability of a regional-scale weather model to simulate extreme precipitation patterns and flooding in central Texas, Weather and Forecasting. *Weather Forecasting*, *23*(6), 1102–1126. https://doi.org/10.1175/2008waf2006082.1

McMillen, J. D., & Steenburgh, W. J. (2015). Impact of microphysics parameterizations on simulations of the 27 October 2010 Great Salt Lake–effect snowstorm. *30*(1), 136–152. https://doi.org/10.1175/waf-d-14-00060.1

Mishra, S. K., & Srinivasan, J. (2010). Sensitivity of the simulated precipitation to changes in convective relaxation time scale. *Paper Presented at Annales Geophysicae, Copernicus GMBH*, *28*, 1827–1846. https://doi.org/10.5194/angeo-28-1827-2010

Mlawer, E. J., Taubman, S. J., Brown, P. D., Iacono, M. J., & Clough, S. A. (1997). Radiative transfer for inhomogeneous atmospheres. RRTM, a validated correlated-k model for the longwave. *Journal of Geophysical Research: Atmospheres*, *102*(D14), 16663–16682. https://doi.org/10.1029/97JD00237

MOIS. (2019). *Ministry of Interior and Safety (MOIS)*. Retrieved from https://www.mois.go.kr/frt/a01/frtMain.do

Molinari, J., & Dudek, M. (1992). Parameterization of convective precipitation in mesoscale numerical models. *Critical Review*, *120*(2), 326–344. https://doi.org/10.1175/1520-0493(1992)120<0326:pocpim>2.0.co;2

Mun, T., Park, C., Kim, G., & Cha, D.-H. (2019). Long-term variability of summer heavy rainfall in the Seoul metropolitan area, *14*(4), 209–219, https://doi.org/10.14383/cri.2019.14.4.209

Noh, Y., Cheon, W. G., Hong, S. Y., & Raasch, S. (2003). Improvement of the K-profile model for the planetary boundary layer based on large eddy simulation data. *Boundary-Layer Meteorology*, *107*(2), 401–427. https://doi.org/10.1023/A:1022146015946

Park, C.-Y., Moon, J.-Y., Cha, E.-J., Yun, W.-T., & Choi, Y.-E. (2008). Recent changes in summer precipitation characteristics over South Korea. *Journal of the Korean Geographical Society*, *43*(3), 324–336.

Park, S. (2014). A unified convection scheme (UNICON). Part I: Formulation. *Journal of the Atmospheric Sciences*, *71*(11), 3902–3930. https://doi.org/10.1175/jas-d-13-0233.1

Prein, A. F., Langhans, W., Fosser, G., Ferrone, A., Ban, N., Goergen, K., et al. (2015). A review on regional convection-permitting climate modeling: Demonstrations, prospects, and challenges. *Reviews of geophysics*, *53*(2), 323–361. https://doi.org/10.1002/2014rg000475

Saito, K., Fujita, T., Yamada, Y., Ishida, J.-i., Kumagai, Y., Aranami, K., et al. (2006). The operational JMA nonhydrostatic mesoscale model. *Monthly Weather Review*, *134*(4), 1266–1298. https://doi.org/10.1175/mwr3120.1

Seo, K.-H., Son, J.-H., & Lee, J.-Y. J. A. (2011). A new look at Changma. *Atmosphere*, *21*(1), 109–121.

Shin, C.-S., & Lee, T.-Y. (2005). Development mechanisms for the heavy rainfalls of 6-7 August 2002 over the middle of the Korean Peninsula. *Journal of the Meteorological Society of Japan. Ser. II*, *83*(5), 683–709. https://doi.org/10.2151/jmsj.83.683

Sims, A. P., Alapaty, K., & Raman, S. (2017). Sensitivities of summertime mesoscale circulations in the coastal Carolinas to modifications of the Kain–Fritsch cumulus parameterization. *Monthly Weather Review*, *145*(11), 4381–4399. https://doi.org/10.1175/mwr-d-16-0047.1

Skamarock, W. C., Klemp, J. B., Dudhia, J., Gill, D. O., Liu, Z., Berner, J., et al. (2019). A description of the advanced research WRF model version 4. *National Center for Atmospheric Research: National Center for Atmospheric Research: Boulder*, 145.

Sun, J., & Lee, T.-Y. (2002). A numerical study of an intense quasi-stationary convection band over the Korean Peninsula. *Journal of the Meteorological Society of Japan. Ser. II*, *80*(5), 1221–1245. https://doi.org/10.2151/jmsj.80.1221

Tokioka, T., Yamazaki, K., Kitoh, A., & Ose, T. J. (1988). The equatorial 30-60 day oscillation and the Arakawa-Schubert penetrative cumulus parameterization. *Journal of the Meteorological Society of Japan. Ser. II*, *66*(6), 883–901. https://doi.org/10.2151/jmsj1965.66.6_883

Wang, W., & Seaman, N. L. (1997). A Comparison study of convective parameterization schemes in a mesoscale model. *Monthly Weather Review*, *125*(2), 252–278. https://doi.org/10.1175/1520-0493(1997)125<0252:Acsocp>2.0.Co

Weisman, M. L., Skamarock, W. C., & Klemp, J. B. (1997). The resolution dependence of explicitly modeled convective systems. *Monthly Weather Review*, *125*(4), 527–548. https://doi.org/10.1175/1520-0493(1997)125<0527:trdoem>2.0.co;2

Wilks, D. S. (2011). *Statistical methods in the atmospheric sciences*. Academic Press.

Yang, M.-J., Chien, F.-C., & Cheng, M.-D. (2000). Precipitation parameterization in a simulated Mei-Yu Front. *Atmospheric, and Oceanic Sciences*, *11*(2), 393–422. https://doi.org/10.3319/tao.2000.11.2.393(a)

Yu, X., & Lee, T.-Y., (2010). Role of convective parameterization in simulations of a convection band at grey-zone resolutions. *Tellus A: Dynamic Meteorology and Oceanography*, *62*(5), 617–632. https://doi.org/10.1111/j.1600-0870.2010.00470.x

Yun, Y., Fan, J., Xiao, H., Zhang, G. J., Ghan, S. J., Xu, K. M., et al. (2017). Assessing the resolution adaptability of the Zhang-McFarlane cumulus parameterization with spatial and temporal averaging. *Journal of Advances in Modeling Earth Systems*, *9*(7), 2753–2770. https://doi.org/10.1002/2017ms001035

Zheng, Y., Alapaty, K., Herwehe, J. A., Del Genio, A. D., & Niyogi, D. J. M. W. R. (2016). Improving high-resolution weather forecasts using the Weather Research and Forecasting (WRF) Model with an updated. Kain–Fritsch scheme. *Monthly Weather Review*, *144*(3), 833–860. https://doi.org/10.1175/mwr-d-15-0005.1